

Cell Tracking according to Biological Needs - Strong Mitosis-aware Random-finite Sets Tracker with Aleatoric Uncertainty

Timo Kaiser¹ Maximilian Schier¹ Bodo Rosenhahn¹

Abstract

Cell tracking and segmentation assist biologists in extracting insights from large-scale microscopy time-lapse data. Driven by local accuracy metrics, current tracking approaches often suffer from a lack of long-term consistency. To address this issue, we introduce an uncertainty estimation technique for neural tracking-by-regression frameworks and incorporate it into our novel extended Poisson multi-Bernoulli mixture tracker. Our uncertainty estimation identifies uncertain associations within high-performing tracking-by-regression methods using problem-specific test-time augmentations. Leveraging this uncertainty, along with a novel mitosis-aware assignment problem formulation, our tracker resolves false associations and mitosis detections stemming from long-term conflicts. We evaluate our approach on nine competitive datasets and demonstrate that it outperforms the current state-of-the-art on biologically relevant metrics substantially, achieving improvements by a factor of approximately 5.75. Furthermore, we uncover new insights into the behavior of tracking-by-regression uncertainty.

1. Introduction

Cell tracking and segmentation algorithms are valuable tools for automating a significant portion of the laborious work required to analyze the output of optical microscopes in biomedical research (Antony et al., 2013). In recent years, leading segmentation approaches (Guerrero Peña et al., 2020; Lalit et al., 2021; Zhu & Meijering, 2021) tend to employ neural networks (NN) that are often inspired by *U-Net* (Ronneberger et al., 2015). In line with this trend, the state-of-the-art method *EmbedTrack* (Löffler & Mikut, 2022) has tackled both the segmentation and tracking problems jointly with a single NN by additionally regressing the

¹Institute for Information Processing, Leibniz University Hanover, Hanover, Germany. Correspondence to: Timo Kaiser <kaiser@tnt.uni-hannover.de>.

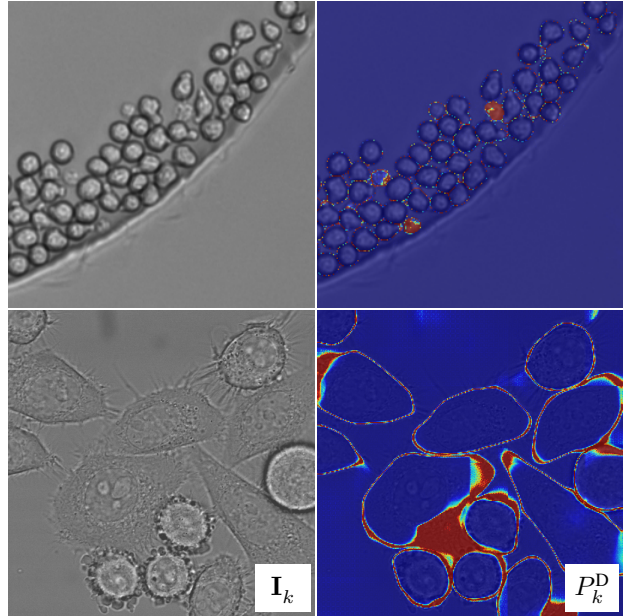


Figure 1. The probability of detection, denoted as P_k^D , reveals uncertain segments in microscopic images I_k . The examples show dense cell populations and red regions indicate uncertain areas in which the predicted detection result may not be reliable. For instance, uncertain areas contain necrotic cells or ambiguous segments in which cell boundaries are not distinguishable.

cell position in the preceding frame, achieving near-perfect benchmark results close to 100% tracking accuracy. Surprisingly, *EmbedTrack* and similar methods focus solely on local cues within two subsequent frames. Revisiting the technical metrics (Bernardin & Stiefelhagen, 2008; Matula et al., 2015) of top tracking benchmarks (Maška et al., 2014; Anjum & Gurari, 2020), the focus on local correctness seems reasonable, because local mistakes like missing segmentations are penalized harder than rare associations errors that corrupt an entire cell trajectory. Unfortunately, this limits the practical usage of algorithms, even though conventional technical metrics suggest that the tracking problem is nearly solved. According to (Maška et al., 2023), there exists a discrepancy between technical metrics and biological metrics (Ulman et al., 2017) that reflect the relevance for biomedical practitioners. These disparities between medical

practitioners’ needs and engineering benchmarks are also highlighted in (Eisenmann et al., 2023).

To bridge the gap between technical and biological measures, this work addresses the problem of missing long-term consistency in modern cell tracking algorithms. We accomplish this by (i) identifying uncertain predictions made by state-of-the-art NNs through uncertainty estimation techniques (Gawlikowski et al., 2023) and (ii) rectifying globally relevant errors using our novel mitosis-aware Poisson multi-Bernoulli mixture (PMBM) Tracker (Granström et al., 2018). Specifically, we initially extend an advanced *test-time augmentation* (Wang et al., 2019) in conjunction with the tracking-by-regression framework *EmbedTrack* to relax the discrete association framework with probability densities and a spatial certainty score for the correct detection of cells. This information is then utilized to evaluate multiple association hypotheses within our novel mitosis-aware PMBM framework that allows non-bijective assignments during mitosis and resolves long-term conflicts a-posteriori. Our approach implicitly replaces the inaccurate Kalman filter motion model of the standard PMBM framework and employs the relaxed association probability density for assignment sampling. Furthermore, we explicitly model mitosis probability to prevent the tracker from detecting improbable mitosis events based on expected cell lifetimes.

We evaluated our method on nine well-established cell tracking datasets (Maška et al., 2014) and demonstrate that we achieve substantial improvements in biologically relevant metrics, by up to a factor of 5.75, compared to the state-of-the-art. Simultaneously, our method preserves the performance of the technical measures without notable differences. This confirms our initial assertion that current algorithms do not align with the requirements of biomedical practitioners but can be improved by establishing long-term consistency.

Our contributions can be summarized as follows:¹

- We estimate the association uncertainty of NNs with a novel test-time augmentation to create an advanced association framework.
- We introduce a novel mitosis-aware PMBM cell tracker to preserve long-term consistency.
- We provide the new state-of-the-art on biologically relevant metrics.

2. Related Work

The prevalent *Tracking-by-Detection* (TbD) paradigm employs a two-stage approach, wherein proposals of object instances (*a.k.a.* detections) obtained from detectors like (Lalit et al., 2022) are associated using strategies such as

greedy matching (Bao et al., 2021). More sophisticated association strategies aim to find a globally optimal solution by constructing a graph and optimizing a minimum-cost flow, for example with the *Viterbi* algorithm (Magnusson et al., 2015). However, the edge costs adhere to the Markov property and only rely on local cues, such as distances (Löffler et al., 2021) or phase correlation (Scherr et al., 2020), disregarding the global cell life cycle. Other methods attempt to maintain global consistency by extracting and clustering appearance embeddings, such as with spatio-temporal Mean Shift (Payer et al., 2019) or with *Mask-RCNN* and Siamese Networks (Chen et al., 2021). The most relevant class of global optimal association strategies in our context includes multi-hypothesis trackers (MHT) (Reid, 1979) and random finite sets trackers (RFS) (Rezatofighi et al., 2015), which have variants like the efficient Poisson multi-Bernoulli mixture tracker (PMBM) (Granström et al., 2018). These tracker re-evaluate multiple hypotheses a-posteriori based on new information, thus having the capacity to use prior sub-optimal hypotheses to resolve errors. In cell tracking, existing RFS model mitosis as a potential hypothesis and score its probability based on local appearance (Nguyen et al., 2021; Hossain et al., 2018) but do not incorporate cell lifetime as a biologically inspired cue.

A more contemporary paradigm is *Tracking-by-Regression* (TbR), where the position and motion of potential objects are regressed jointly based on local cues with NNs (Bergmann et al., 2019). For example, *EmbedTrack* (Löffler & Mikut, 2022) introduces a multitask regression head that estimates instance segmentation, center, and motion of cell detections. By its very nature, this paradigm can only preserve local dependencies. Nevertheless, TbR proves to be an effective and competitive data-driven tracking approach, leading to state-of-the-art results on technical tracking metrics.

Without a focus on tracking, a lot of research is dedicated to estimating the uncertainty in NN-driven predictions. For instance, in medical imaging, Bayesian approaches (Wang & Lukasiewicz, 2022) are employed to approximate epistemic uncertainty or test-time augmentation (Wang et al., 2019) is used to quantify aleatoric uncertainty. However, NN-derived uncertainty estimation is rarely applied, neither in cell tracking nor general object tracking. To the best of our knowledge, the only commonly utilized NN-derived uncertainty in tracking pertains to the probability of being clutter to filter detection noise, as seen in (Hornakova et al., 2021) and other works. A few approaches employ advanced strategies like normalizing flows (Mancusi et al., 2023) for optimizing association during training or fuzzy logic (Stegmaier & Mikut, 2017), which is unrelated to NNs.

¹Code at <https://github.com/TimoK93/BiologicalNeeds>

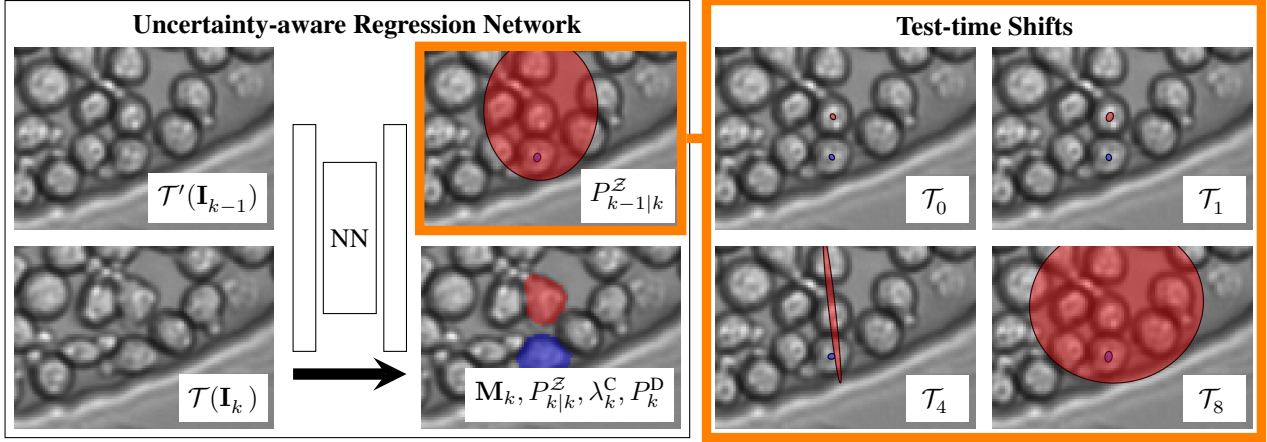


Figure 2. Our uncertainty-aware tracking-by-regression framework, applied to *EmbedTrack*. The input comprises two consecutive images \mathbf{I}_{k-1} and \mathbf{I}_k with test-time augmentation \mathcal{T} and \mathcal{T}' . The NN estimates instance segmentations \mathbf{M}_k , along with their clutter probability λ_k^C , Gaussian distributed motion $P_{k-1|k}^Z$ and position $P_{k-1|k}^Z$, and the pixelwise probability of detection P_k^D . The orange box shows the Gaussian distributed motion estimation with different shifts s during test-time augmentation \mathcal{T}_s . For clarity, we only visualize two cells.

3. Uncertainty in Tracking-by-Regression

Given an image sequence $\mathcal{I} = \{\mathbf{I}_k\}_{k=1}^K$ containing images $\mathbf{I}_k \in \mathbb{R}^{H \times W}$ with $H \times W$ pixels at time k , the task of cell instance segmentation is to find and represent every visible cell with a discrete map $\mathbf{M}_k \in \mathbb{N}_0^{H \times W}$ that labels a pixel depending on whether it belongs to a specific cell instance or background. To extend the task to cell tracking, an additional step involves the association of segments between consecutive frames, such that all segmented areas that belong to the same specific cell instance are labeled with the same unique identifier. Furthermore, cell division, known as mitosis, must be detected and indicated through a parent-daughter relationship.

Methods that follow the TbR paradigm usually solve the task by estimating the existence of objects and their motion jointly with a single NN based on subsequent images $(\mathbf{I}_{k-1}, \mathbf{I}_k)$. Our baseline *EmbedTrack* (Löffler & Mikut, 2022) estimates the pixelwise probability of belonging to a cell segment $\mathbf{D}_k \in (0, 1)^{H \times W}$, the relative offset to the corresponding cell-centroid $\mathbf{O}_k^S \in (-1, 1)^{H \times W \times 2}$, and a clustering-bandwidth $\mathbf{S}_k \in (0, 1)^{H \times W}$. The estimation of \mathbf{D}_k , \mathbf{O}_k^S , \mathbf{S}_k are jointly used to cluster 2D cell-centroids $\mathcal{Z}_k = \{\mathbf{z}_k^j\}_{j=1}^{N_k^Z}$ and cell instance segments \mathbf{M}_k . Furthermore, a motion offset $\mathbf{O}_k^T \in (-1, 1)^{H \times W \times 2}$ that points to the position of the cell-centroid in the preceding frame \mathbf{I}_{k-1} is regressed for every pixel. The offsets $\bar{\mathbf{z}}_k^j \in \mathbf{O}_k^T$ determined by the position of the corresponding \mathbf{z}_k^j are equivalent to the motion of cell j . Finally, *EmbedTrack* solves the tracking task with nearest-neighbor matching between the warped detections $\mathcal{Z}_{k-1|k} = \{\mathbf{z}_{k-1|k}^j = \mathbf{z}_k^j + \bar{\mathbf{z}}_k^j\}_{j=1}^{N_k^Z}$ in frame k and previous detections \mathcal{Z}_{k-1} in frame $k-1$.

In the next sections, we introduce our method and enhance

EmbedTrack to derive uncertainty estimations that are used in an extended tracking strategy in Section 4. We want to emphasize that the concepts apply to arbitrary TbR frameworks. Our modified *EmbedTrack* is visualized in Figure 2.

Test-Time Augmentation is a widely used strategy to reduce data noise during inference by applying a set of transformations \mathcal{T} to the input image \mathbf{I} and averaging the inferred estimations (Wang et al., 2019). *EmbedTrack* applies rotations of 0, 90, 180, and 270 degrees and reflections, resulting in a set of $|\mathcal{T}| = 8$ Euclidean transformations. It is worth mentioning that transformations are equally applied to \mathbf{I}_{k-1} and \mathbf{I}_k before inference.

While this strategy tackles geometrical variances in instance segmentation, motion regression networks that implicitly perform association based on visual cues suffer from two major problems: Cell appearance is similar within a population and can change drastically between consecutive frames (see Figure 2). Since a reliable assignment is sometimes not possible even for humans, we suspect that the regression network performs an uncertain and heuristic assignment like simple nearest-neighbor matching in those cases. To tackle heuristic behavior, we add multiple transformations on top of \mathcal{T} that keep \mathbf{I}_k unchanged but shift \mathbf{I}_{k-1} for s pixels in all directions. The resulting set of transformations $\mathcal{T}' = \{\mathcal{T}_{s_1}, \dots, \mathcal{T}_{s_n}\}$ can lead to varying motion estimations because the nearest neighbors can change due to the shift. This indicates uncertainty. To estimate the uncertainty in further steps, we calculate pixel-wise (co)variances of the estimation, denoted as $\Sigma(\mathbf{D}_k) \in \mathbb{R}_+^{H \times W}$, $\Sigma(\mathbf{O}_k^S) \in \mathbb{R}_+^{H \times W \times 2 \times 2}$, and $\Sigma(\mathbf{O}_k^T) \in \mathbb{R}_+^{H \times W \times 2 \times 2}$. Note that $\Sigma(\mathbf{D}_k)$ is calculated on logits to induce linearity.

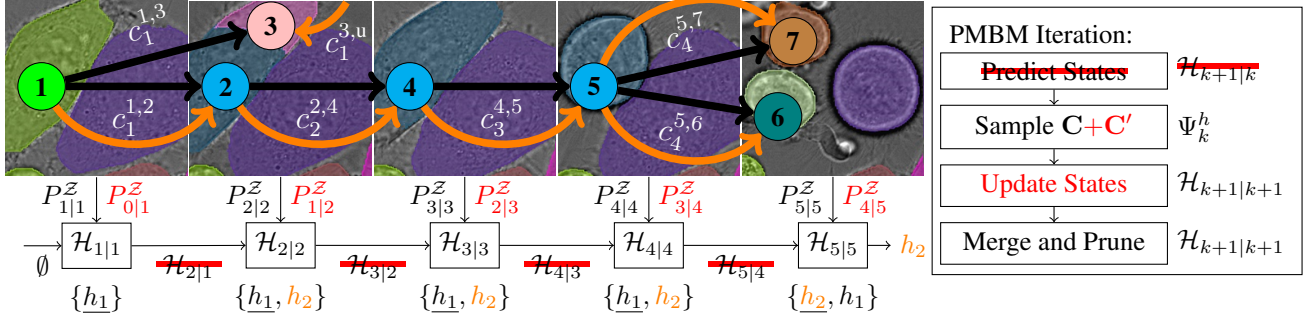


Figure 3. Schematic overview of our PMBM tracking framework. Red elements highlight our contributions applied to the vanilla PMBM and the right flow chart illustrates a PMBM iteration. We use position $P_{k|k}^{\mathcal{Z}}$ and motion estimation $P_{k-1|k}^{\mathcal{Z}}$ to update the hypotheses $\mathcal{H}_{k+1|k}$ to $\mathcal{H}_{k+1|k+1}$. The sets $\mathcal{H}_{k|k}$ containing h_1 and h_2 indicate hypotheses for an example image sequence, in which an over-segmentation occurs in frame $k = 2$. The underlining indicates the most likely hypothesis. Our PMBM framework enables us to rectify the falsely detected mitosis in $k = 2$ with posterior knowledge from $k = 5$, as it identifies an implausible short life cycle for the blue cell.

Uncertainty in Position and Motion. By now, the estimated position and motion of detection j is described by 2D vectors $\mathbf{z}_{k|k}^j$ and $\mathbf{z}_{k-1|k}^j$ that only allow simple association like nearest-neighbor matching with handcrafted distance metrics. To consider motion estimation uncertainty in an advanced tracker, we derive multivariate Gaussian densities

$$P_{k-1|k}^{j,\mathcal{Z}}(\cdot) = \mathcal{N}(\cdot; \mu_{k-1|k}^{j,\mathcal{Z}}, \Sigma_{k-1|k}^{j,\mathcal{Z}}) \quad (1)$$

for the spatial position in the former frame. We calculate $\mu_{k-1|k}^{j,\mathcal{Z}}$ and $\Sigma_{k-1|k}^{j,\mathcal{Z}}$ by merging a Gaussian mixture model (GMM) from the estimated output of *EmbedTrack*. The GMM consists of the multivariate Gaussians

$$\{(\mathbf{D}_{k,\mathbf{p}}, \mathcal{N}(\cdot; \mathbf{p} + \mathbf{O}_{k,\mathbf{p}}^T, \Sigma(\mathbf{O}_{k,\mathbf{p}}^T)) \mid \forall \mathbf{p} : \mathbf{M}_{k,\mathbf{p}} = j)\} \quad (2)$$

where \mathbf{p} describes the position of pixels in \mathbf{M}_k that belong to cell j . The spatial position distribution $P_{k|k}^{j,\mathcal{Z}}(\cdot)$ in the current frame is derived in the same manner by substituting \mathbf{O}_k^T with \mathbf{O}_k^S in Equation (2). Merging a GMM into a single multivariate Gaussian is described in the Appendix, Section A.

Probability of Clutter. Tracking systems rely on the quality of their input. The probability that a detection j in frame k is a false detection (*a.k.a.* clutter) is denoted as $\lambda_k^{C,j}$. We estimate $\lambda_k^{C,j}$ by using the probability of confusion $1 - \mathbf{D}_{k,\mathbf{p}}$ at pixel $\mathbf{p} = \mu_{k|k}^{j,\mathcal{Z}}$.

Probability of Detection. Denoted as $P_k^D(\mathbf{p}) = 1 - P_k^{MD}(\mathbf{p})$, the probability of detection describes the likelihood of having a certain segmentation score $\mathbf{D}_{k,\mathbf{p}}$ at pixel \mathbf{p} . We estimate the probability of misdetection

$$P_k^{MD}(\mathbf{p}) = S\left(l(\mathbf{D}_{k,\mathbf{p}}) + \sigma_{k,\mathbf{p}}^D\right) - S\left(l(\mathbf{D}_{k,\bar{x}}) - \sigma_{k,\mathbf{p}}^D\right) \quad (3)$$

where S denotes the Sigmoid function, l the logit function, and $\sigma_{k,\mathbf{p}}^D = \sqrt{\Sigma(\mathbf{D}_k)}_{\mathbf{p}}$ the standard deviation at pixel \mathbf{p} . Thus, Equation 3 describes a 68% confidence interval.

4. Mitosis-aware Random Finite Sets Tracker

This section introduces an extended, theoretically global optimal Poisson Multi-Bernoulli Mixture tracker (PMBM), that resolves errors a-posteriori based on long-term conflicts. An example of such errors is visualized in Figure 3, in which the black track hypothesis seems more plausible without the posterior knowledge from frame 5.

The vanilla PMBM tracker (Granström et al., 2018) solves the tracking problem by finding the maximum of the state density distribution $\mathcal{PMBM}_{k|k}(\cdot)$. This distribution is mainly defined by a multi-Bernoulli mixture

$$\mathcal{H}_{k|k}(\cdot) = \left\{ \left(l_{k|k}^h, \left\{ \left(r_{k|k}^{i,h}, \mathcal{N}(\cdot; \mu_{k|k}^{i,h}, \Sigma_{k|k}^{i,h}) \right) \right\}_i^{N_k^h} \right) \right\}_h^{H_k} \quad (4)$$

representing possible hypotheses of objects that were detected at least once until frame k . It is structured in H_k hypotheses per frame k , in which $l_{k|k}^h$ describes the log-likelihood of hypothesis h that consists of N_k^h potential objects. Every object i has a 2D Gaussian spatial density defined by mean $\mu_{k|k}^{i,h}$ and covariance $\Sigma_{k|k}^{i,h}$ as well as a probability of existence $r_{k|k}^{i,h}$. Initialized with $\mathcal{H}_{0|0} = \{(1, \emptyset)\}$, the sets $\mathcal{H}_{k+1|k+1}$ are deduced by performing the following steps on every hypothesis $h \in \mathcal{H}_{k|k}$ independently.

First, the expected states of h in $k+1$ are predicted using a linear Kalman filter (Kalman, 1960) motion model, such that $h \in \mathcal{H}_{k+1|k}$. Then, given a set of detections \mathcal{Z}_{k+1} , association costs $c_k^{j,i,h}$ between detections $j \in \mathcal{Z}_{k+1}$ and known objects $i \in h$ as well as costs $c_k^{j,u,h}$ for keeping j unassigned are arranged in an assignment cost matrix \mathbf{C}_k^h .

The most likely assignments $\psi \in \Psi_k^h$ are created with \mathbf{C}_k^h using Murty’s sampling (Murty, 1968) and used to create updated hypotheses $f(h, \mathcal{Z}_{k+1}, \psi, P^D, \lambda^C) \in \mathcal{H}_{k+1|k+1}$. During the update f , the states of h are updated according to Kalman and the assigned detections from \mathcal{Z}_{k+1} . Also, the likelihood $l_{k+1|k}^h$ is updated to $l_{k+1|k+1}^h$ with the probability that ψ is correct. The probability can be calculated based on the parameters of h and \mathcal{Z}_{k+1} as well as with the handcrafted and usually constant probability of detection P^D and clutter probability λ^C .

Since H_k is exponentially growing and impairs practical computation, hypotheses with low probability are pruned until $H_k \leq H_{\max}$. Also, sampling from \mathbf{C}_k^h is cut down to the most likely hypotheses such that $|\Psi_k^h| = A_{\max}$. Furthermore, multiple hypotheses can be merged if they are describing approximately the same state. The labeled tracking result for an image sequence with K images as described in Section 3 can trivially be reconstructed by inversely tracing the most likely hypothesis in $\mathcal{H}_{K|K}$ down to its ancestor in $\mathcal{H}_{0|0}$.

Due to its complexity, we briefly summarized the concept of the PMBM and skipped details irrelevant to our contributions. For readers interested in the entire framework or re-implementing the PMBM, we refer to our detailed recap in the Appendix, Section C.

The PMBM tracker suffers from several drawbacks for cell tracking: There is no accurate motion model due to the often unpredictable cell motion in time-lapse videos and the one-to-one association does not allow cell mitosis. Thus, the following sections introduce (1) our novel motion-containing PMBM tracker based on our uncertainty-aware regression system that (2) also incorporates mitosis, extended with our novel cell cycle preserving mitosis costs. Furthermore but without giving more details in the following, we (3) replace the usually handcrafted probability of detection and clutter with our uncertainty-based $P_k^D(p)$ and $\lambda_k^{C,j}$ introduced in the former section. The PMBM framework with and without our contributions (1) and (2) is visualized in Figure 3.

4.1. Implicit Motion Model

Instead of only using the spatial position of detection proposals, we propose to use the entire output of our uncertainty-aware regression model from Section 3 such that

$$\mathcal{Z}_{k+1} = \left\{ \left(\lambda_{k+1}^{C,j}, P_{k+1|k+1}^{j,\mathcal{Z}}(\cdot), P_{k+1|k+1}^{j,\mathcal{Z}}(\cdot) \right) \right\}_{j=1}^{N_{k+1}^{\mathcal{Z}}} \quad (5)$$

This allows us to utilize a solid motion model implicitly in \mathcal{Z}_{k+1} that makes the prediction step obsolete. Consequently, we also do not apply the Kalman filter during update f . Instead, we use the estimation of the usually high-performing regression model and update the object positions with $\mu_{k+1|k+1}^{i,h} = \mu_{k+1}^{j,\mathcal{Z}}$ and $\Sigma_{k+1|k+1}^{i,h} = \Sigma_{k+1}^{j,\mathcal{Z}}$. Objects that are not assigned to a detection keep their mean but we

Table 1. Ablation studies conducted using public training data containing complete cell life cycles. We set sampling parameter $A_{\max} = 1$ or $H_{\max} = 1$, deactivated mitosis costs $c_k^{M,i,h} = 0$, and substituted our implicit motion model with the standard Kalman filter. Our method performs substantially better on long sequences with complex scenarios if all contributions are applied jointly.

	CCA [%]↑	Ours	$A_{\max} = 1$	$H_{\max} = 1$	$c_k^{M,i,h} = 0$	Kalman
Dataset	BF-C2DL-HSC	73.01	53.45	54.47	58.68	10.50
	BF-C2DL-MuSC	51.25	41.27	37.86	45.02	15.86
	PhC-C2DL-PSC	77.95	76.50	77.13	75.04	19.41
	Fluo-N2DH-SIM+	42.63	42.86	43.85	41.47	31.92
	Fluo-N2DL-HeLa	88.54	87.04	87.84	88.90	25.91
	TF [%]↑	Ours	$k_S = 1$	$k_H = 1$	$c_k^{M,i,h} = 0$	Kalman
Dataset	BF-C2DL-HSC	88.61	86.63	83.30	86.48	28.62
	BF-C2DL-MuSC	71.78	71.29	70.77	72.32	45.67
	PhC-C2DL-PSC	87.22	87.31	87.28	87.16	17.681
	Fluo-N2DH-SIM+	92.56	93.16	92.65	92.63	86.93
	Fluo-N2DL-HeLa	94.71	94.37	94.46	94.51	59.22

increase the covariance $\Sigma_{k+1|k+1}^{i,h} = \Sigma_k^{i,h} + \text{Diag}(\bar{\sigma}_m^2)$ by the mean cell motion per frame $\bar{\sigma}_m$ on the diagonal.

4.2. Mitosis-aware Association

The vanilla PMBM does not allow that object i from $h \in \mathcal{H}_{k+1|k}$ has an association with multiple detections j_1 and j_2 from measurement \mathcal{Z}_{k+1} . This is caused by the design of the cost matrix \mathbf{C}_k^h for the assignment problem, in which only one association per row and column is allowed. The standard cost matrix is defined by two submatrices: $\mathbf{C}_k^h = [\mathbf{C}_k^{j,i,h} \mid \text{Diag}_{\infty}(c_k^{j,u,h})]$. Assuming N_k^h objects and $N_{k+1}^{\mathcal{Z}}$ detections, the elements of $\mathbf{C}_k^{j,i,h} \in \mathbb{R}^{N_{k+1}^{\mathcal{Z}} \times N_k^h}$ in row j and column i are filled with the association costs $c_k^{j,i,h}$ between i and j , and $\text{Diag}_{\infty}(c_k^{j,u,h}) \in \mathbb{R}^{N_{k+1}^{\mathcal{Z}} \times N_{k+1}^{\mathcal{Z}}}$ is a diagonal matrix with the costs $c_k^{j,u,h}$ for keeping j unassigned on the diagonal and infinity otherwise. To allow the assignment of j_1 and j_2 to an object i during cell mitosis, we add a submatrix $\mathbf{C}_k^{j_2,i,h}$ to the right, such that

$$\mathbf{C}_k^h = \left[\mathbf{C}_k^{j_1,i,h} \mid \text{Diag}_{\infty}(c_k^{j_1,u,h}) \mid \mathbf{C}_k^{j_2,i,h} = \mathbf{C}_k^{j_1,i,h} \right] \quad (6)$$

Now, if the costs $c_k^{j_1,i,h}$ and $c_k^{j_2,i,h}$ are relatively small, solving the assignment problem leads to an assignment of j_1 in $\mathbf{C}_k^{j_1,i,h}$ and j_2 in $\mathbf{C}_k^{j_2,i,h}$ or vice versa. The costs $c_k^{j_1,i,h}$ and $c_k^{j_2,i,h}$ can be derived using the spatial distributions of the detections in \mathcal{Z}_{k+1} and the parameters of $\mathcal{PMBM}_{k+1|k}$. To do so, the position parameters $\mu_{k+1}^{j,\mathcal{Z}}$ and $\Sigma_{k+1}^{j,\mathcal{Z}}$ of the vanilla PMBM approach need to be replaced by the motion parameters $\mu_{k+1}^{j,\mathcal{Z}}$ and $\Sigma_{k+1}^{j,\mathcal{Z}}$ in Equations (20), (21), and (22) of the vanilla PMBM recap (Section C, Appendix).

4.3. Mitosis Costs

Even with the former modifications, the PMBM framework does not incorporate biological knowledge about the cell life cycle. Thus, we add extra costs $\mathbf{C}_k^{M,i,h}$ to $\mathbf{C}_k^{j,i,h}$ to avoid

Table 2. Benchmark on biological measures on the test data following the *Cell Tracking Challenge* (Maška et al., 2023). Colored cells represent the performance of the top #k state-of-the-art methods. The baseline rows compare the heuristic association of the standard *EmbedTrack* (Löffler & Mikut, 2022) to our global optimal association approach. Numbers highlighted in **bold** indicate that we surpass the baseline, and underlined numbers indicate that our approach is the new state-of-the-art over all participating methods. The N/A flag denotes that the metric is not available. Corresponding affiliations and references to the name tags can be found in the Appendix, Table 5.

[%] ↑		BF-C2DL-HSC	BF-C2DL-MuSC	DIC-C2DL-HeLa	Fluo-C2DL-MSc	Fluo-N2DH-GOWT1	Fluo-N2DL-HeLa	PhC-C2DH-U373	PhC-C2DL-PSC	Fluo-N2DH-SIM+	Method
Frames		1763	1375	114	47	91	91	114	299	109	KIT-GE (1)
CT	Top #1	5.94	5.32	16.88	29.29	36.58	67.45	57.33	17.13	59.58	KIT-GE (2)
	Top #2	5.4	1.65	12.20	20.29	34.13	63.34	50.40	16.79	58.53	KIT-GE (3)
	Top #3	4.42	1.53	9.08	15.14	31.43	59.59	50.22	14.23	53.09	KIT-GE (4)
	Baseline	5.94	1.00	12.20	6.79	27.26	58.76	50.22	14.23	59.88	KTH-SE (1)
	Ours	<u>16.2</u>	2.0	25.9	11.1	29.7	68.0	66.7	17.2	62.3	KTH-SE (3*)
TF	Top #1	62.26	68.46	80.93	75.29	94.16	98.05	100.0	84.16	93.66	KTH-SE (5)
	Top #2	59.62	68.16	75.30	74.96	93.57	96.95	99.85	83.65	92.72	BGU-IL (1)
	Top #3	57.14	63.49	73.90	68.12	89.01	96.85	99.82	82.65	91.71	BGU-IL (5)
	Baseline	62.26	68.16	75.30	59.59	84.00	96.95	97.07	82.65	93.66	HD-GE (BMCV) (1)
	Ours	<u>75.7</u>	73.5	82.2	63.3	90.1	97.3	97.1	83.7	94.6	HD-GE (IWR)
BC(i)	Top #1	44.05	65.10	N/A	N/A	N/A	88.21	N/A	60.04	92.16	FR-GE (2)
	Top #2	32.46	55.07	N/A	N/A	N/A	88.12	N/A	57.59	91.79	HKI-GE (5)
	Top #3	27.68	39.20	N/A	N/A	N/A	81.10	N/A	53.58	89.67	THU-CN (2)
	Baseline	32.46	24.68	N/A	N/A	N/A	77.09	N/A	48.17	92.16	TUG-AT
	Ours	56.4	68.0	N/A	N/A	N/A	86.9	N/A	59.6	91.4	USYD-AU
CCA	Top #1	56.33	85.18	N/A	N/A	N/A	93.12	N/A	85.34	94.76	ND-US (1)
	Top #2	51.79	34.02	N/A	N/A	N/A	91.37	N/A	64.89	91.71	DREX-US
	Top #3	43.33	25.37	N/A	N/A	N/A	89.71	N/A	63.49	90.52	IMCB-SG (1)
	Baseline	12.23	11.82	N/A	N/A	N/A	62.75	N/A	34.75	85.29	UVA-NL
	Ours	56.4	68.0	N/A	N/A	N/A	86.9	N/A	59.6	91.4	HIT-CN (1)

Table 3. Impact of shifts with s pixels on motion estimation when adding \mathcal{T}_s to standard augmentations \mathcal{T}_0 . We present the average standard deviation in relative image lengths without any shift in column \mathcal{T}_0 . The values in columns \mathcal{T}_1 to \mathcal{T}_8 indicate the amplification relative to \mathcal{T}_0 , highlighting the effect caused by shifts.

Dataset	[Relative Image Size]	Shift				
		\mathcal{T}_0	\mathcal{T}_1	\mathcal{T}_2	\mathcal{T}_4	\mathcal{T}_8
BF-C2DL-HSC	0.30%	×1.38	×2.14	×5.00	×25.22	
BF-C2DL-MuSC	2.08%	×1.00	×1.04	×1.07	×1.21	
Fluo-N2DL-HeLa	0.43%	×1.01	×1.03	×1.12	×1.76	
PhC-C2DL-PSC	0.36%	×1.02	×1.12	×1.46	×3.35	
Fluo-N2DH-SIM+	0.54%	×1.03	×1.18	×1.32	×1.55	
DIC-C2DH-HeLa	2.05%	×1.03	×1.06	×1.14	×1.34	
Fluo-C2DL-MSc	3.25%	×1.03	×1.04	×1.00	×1.05	
Fluo-N2DH-GOWT1	0.53%	×1.05	×1.26	×1.42	×1.72	
PhC-C2DH-U373	0.76%	×1.11	×1.18	×1.27	×1.33	

unlikely mitosis detections such that $C_k^{j,i,h} = C_k^{j,i,h} + C_k^{M,i,h}$. A value $C_k^{M,i,h}$ in column i reflects the probability that cell i from hypothesis h splits in this step. We set

$$C_k^{M,i,h} = \begin{cases} -\log\left(\frac{k_M - \text{Age}(i)}{k_M}\right) & \text{if } \text{Age}(i) < k_M \\ 0 & \text{if } \text{Age}(i) \geq k_M \\ 0 & \text{if } \text{Age}(i) = \emptyset \end{cases} \quad (7)$$

with the current lifetime $\text{Age}(i)$ of the cell (that also can be unknown!) and a manually defined hyperparameter k_M that reflects a reasonable minimal lifetime of cells. Adding these costs penalizes hypotheses that cause implausible short cell life cycles. For example, in Figure 3, even if the black

hypothesis is more likely before frame 5, the mitosis in frame 5 causes high association costs. This causes the brown track without mitosis in frame 2 to appear more likely a-posteriori. We want to emphasize, that a more sophisticated rating function than given in Equation (7) is not part of this work but could be investigated in the future.

5. Experiments

This section presents experimental results analyzing our uncertainty estimation and tracking framework. We evaluated our method on nine publicly available and competitive datasets provided by the *Cell Tracking Challenge* (Maška et al., 2023). These datasets encompass a wide range of sequence lengths and complexities.

Since our method aims to enhance long-term consistencies essential for monitoring entire cell life cycles, we assess its performance using biologically relevant metrics (Ulman et al., 2017) reported by the *Cell Tracking Challenge*. Specifically, we report *Complete Tracks* (CT), *Track Fractions* (TF), *Branching Correctness* (BC(i)), and *Cell Cycle Accuracy* (CCA). CT indicates the fraction of tracks that are entirely reconstructed without error, while TF reports the average continuously correct reconstructed fraction of a track. For evaluating mitosis detection, BC(i) indicates the fraction of correctly detected cell splits and CCA is the overlap of predicted and ground truth life cycle distribution.

To ensure a fair comparison, we employ the code and pre-

trained models of *EmbedTrack* (Löffler & Mikut, 2022) without any modification or re-training and only apply our uncertainty estimation strategy. Thus, we refer to *EmbedTrack* as our baseline. If not stated otherwise, our extended PMBM tracker is implemented using hyperparameters $A_{\max} = 7$, $H_{\max} = 150$, and k_M is dataset dependent. We merge hypotheses if their states are equal. After tracking, we remove very small tracks and interpolate at gaps. More details for re-implementation are given in the Appendix, Section B. The code is publicly available (see page 2).

5.1. Quantitative Results

Our method is specifically designed to enhance tracking results in long and complex scenarios by effectively resolving long-term conflicts through the introduction of mitosis costs. To evaluate this capability, we present the results obtained on nine diverse datasets, assessed using the evaluation server of the *Cell Tracking Challenge*. These results are summarized in Table 2. Compared to the baseline *EmbedTrack*, our method exhibits a substantial improvement in metrics, particularly for complex datasets, with improvements up to a factor of $\times 5.75$ (CCA, BF-C2DL-MuSC). Our method emerges as the new state-of-the-art in 7 out of 9 datasets on the biological metrics benchmark compared to all other competitors in the challenge. The improvement diminishes as data complexity decreases, aligning with our method design, as smaller datasets rarely include entire cell life cycles.

Another noteworthy observation pertains to the discrepancy between the reported biologically relevant metrics in Table 2 and the additionally evaluated technical metrics shown in the Appendix, Table 4. Both our approach and the baseline achieve technical metrics that are close to optimal, with differences largely attributable to noise. This underscores the concern stated in Section 1 that technical metrics often do not reflect the needs of biologists. Our method addresses this issue by prioritizing long-term consistency and effectively resolving specific mitosis errors introduced by high-performing regression networks. These errors, while having a minimal impact on technical metrics, significantly influence biologically relevant metrics.

5.2. Uncertainty Estimation

During test-time augmentation, we apply transformations \mathcal{T}_s to shift the image \mathbf{I}_{k-1} by s pixels. This practice helps to avoid heuristic nearest-neighbor matching by identifying uncertain predictions. The impact of various augmentations \mathcal{T}_s is illustrated in Figure 2, where shifts of 0, 1, 4, and 8 pixels are applied to an image containing a crowded cell population with approximately 20×20 pixels per cell.

There are two cells visualized: a cell with a strong appearance change (red) and an easy-to-reidentify cell (blue). When only applying \mathcal{T}_0 , we observe small variances in both

motion estimations in $P_{k-1|k}^Z$, indicating low uncertainty. This confirms the assumption that the default strategy leads to very certain predictions in uncertain environments. However, applying a small translation of 1 pixel in \mathcal{T}_1 leads to a small increase in uncertainty, while a shift of 4 pixels in \mathcal{T}_4 results in significantly growing variances for the red cell. This allows multiple plausible associations during tracking. Lastly, applying \mathcal{T}_8 leads to drastically increasing variance for the uncertain cell, but is small for the certain blue cell. More samples are shown in the Appendix, Figures 5-7.

To quantify the impact of shifts on different datasets, Table 3 presents the average standard deviation in relative image size. In datasets with crowded populations and relatively small cells like BF-C2DL-HSC, variances heavily increase, while they continue to grow, although to a lesser extent, for the less crowded PhC-C2DL-PSC dataset. In contrast, datasets with large cells and unambiguous association problems like Fluo-C2DL-MSC do not significantly change in variances with larger shifts. The analysis shows that the regressor remains stable and safe in simple environments. However, the proposed uncertainty estimation is crucial to avoid errors in complex scenarios. These observations provide valuable insights about applications where our approach can be most beneficial.

Our proposed probability of detection P_k^D is visualized in Figures 1, with more examples in Figure 8 to 10 in the Appendix. The spatial probability map allows us to replace the handcrafted and constant P_k^D commonly used in the vanilla PMBM framework. As qualitatively shown in the examples, P_k^D is responsive to areas with ambiguous appearance, for example as in areas with necrotic cells.

5.3. Ablations

The proposed method is a sophisticated system that addresses potential errors by integrating multiple concepts. In the following ablations applied on training data with publicly available ground truth, summarized in Table 1, we explore the strengths, weaknesses, and gain further insights. To assess the impact of our method, we conducted the following experiments: (1) setting the number of sampled hypotheses per association to $A_{\max} = 1$, (2) limiting the total number of hypotheses after pruning to $H_{\max} = 1$, (3) removing our introduced mitosis costs $C_k^{M,i,h}$, and (4) substituting our motion estimation with a Kalman filter, as described in Appendix, Section C. We evaluated these experiments using training data for datasets with complete cell cycles and reported the biological metrics that are least susceptible to noise. In settings (1) and (2), where we did not evaluate multiple hypotheses, the results for long and complex image sequences dropped substantially down by around 20%. This drop is reasonable since the framework is forced to preserve the local optimal hypothesis and cannot resolve long-term

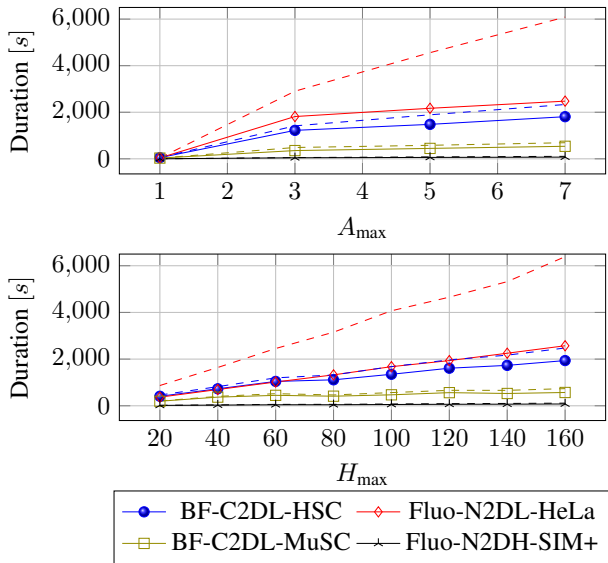


Figure 4. Runtime of our regressed motion model (solid line) compared to the Kalman filter (dashed line) with varying values of the sampling parameter A_{\max} and H_{\max} . Our system shows greater efficiency, primarily because it involves fewer sampling hypotheses caused by more hypotheses that can be merged.

errors, which are most relevant in very long sequences like in BF-C2DL-HSC and BF-C2DL-MuSC. Similar results can be observed without explicit mitosis costs in setting (3). However, $C_k^{M,i,h}$ does not have an observable impact on short sequences and also carries along new noise into the system. To preserve reasonable cell life cycles that increase CCA, seemingly some false associations that can decrease TF are accepted in some datasets. The impact of these false associations is marginal and causes only small differences in TF. Setting (4) shows that the naive Kalman filter is not a suitable motion model to induce long-time consistency. We conclude that motion estimation based on visual cues should be preferred. The main conclusions of this experiment are, that all of our proposed contributions need to be combined to observe state-of-the-art results. Additionally, we demonstrate that our method is particularly well-suited for applications involving long sequences and complex scenarios. It’s important to note that the impact on unseen test data is expected to be even stronger, as training data could potentially be memorized during training.

5.4. Runtime

Compared to the greedy association strategy applied in our baseline *EmbedTrack*, the higher accuracy of a PMBM tracker is paid with a higher computational complexity. However, in Figure 4, we compare the processing time of our uncertainty-aware motion model with the standard Kalman filter on various datasets, varying the maximal number of hypotheses after pruning H_{\max} and the number of

sampled associations A_{\max} .

Our uncertainty-aware motion model consistently outperforms the Kalman filter in processing speed across all settings. While the advantage is marginal in scenarios with fewer cells per frame (BF-C2DL-MuSC and Fluo-N2DL-SIM+), there is a large performance gain in crowded scenarios (BF-C2DL-HSC and Fluo-N2DL-HeLa). This can be explained by the computation of Kalman but also because of the reduction process during sampling in our method: A high certainty in the motion prediction leads to a small number of plausible associations. Thus, association sampling stops without the full amount of A_{\max} new hypotheses per hypothesis in the preceding frame. Furthermore, our object states from \mathcal{H}_k are restricted to have the same state as detections from the measurement \mathcal{Z}_k . This increases the likelihood of merging equal hypotheses. For instance, with default settings and Kalman in sequence 1 of the Fluo-C2DL-Hela dataset, 14 401 of 92 555 hypotheses are merged. Our approach merges 30 406 of 91 288 hypotheses.

Both methods exhibit approximately linear growth in processing time with an increasing number of hypotheses. Given the data acquisition time of several days, the processing time is negligible. The computations were performed on a desktop PC with an Intel i9-9900K CPU running at $16 \times 3.60\text{GHz}$. It is important to note that we only consider the runtime of the PMBM tracker without *EmbedTrack*.

6. Conclusion

This paper introduces a novel cell tracking framework that merges the strong local performance of neural tracking-by-regression frameworks with the global optimal assignment strategy of PMBM trackers. This fusion is achieved by estimating the uncertainty of the neural regressor and expanding the PMBM assignment problem formulation to incorporate mitosis costs. We demonstrate that this approach surpasses the current state-of-the-art on various competitive datasets without additional data or re-training. Our ablations also provide insights into situations where long-term consistency is essential and when heuristic tracking-by-regression approaches are also suitable.

Building upon this work, future approaches have the potential to further enhance long-term consistency. For instance, evaluating more complex distributions like Gaussian mixtures to model motion uncertainty, or sampling multiple detection hypotheses in uncertain regions could broaden the search space of the PMBM. We hope that this work leads to more awareness about the importance of long-term consistency in the community of cell tracking.

Impact Statement

This paper presents work aimed at enhancing awareness of long-term consistency within the cell tracking community, as well as improving the performance of tracking methods. The proposed tracking algorithm is specifically designed to estimate and incorporate the uncertainty of the underlying machine-learning model. It is applied to the output of Tracking-by-Regression models which, depending on the selected model, may be considered a black box. When selecting an algorithmic pipeline for tracking, practitioners should ensure that it meets their requirements regarding explainability, biases, generalization, and other factors they must comply with in their field of research to prevent negative societal consequences.

References

- Anjum, S. and Gurari, D. CTMC: Cell tracking with mitosis detection dataset challenge. In *Conference on Computer Vision and Pattern Recognition Workshops*, 2020. doi: 10.1109/CVPRW50498.2020.00499.
- Antony, P. P. M. A., Trefois, C., Stojanovic, A., Baumuratov, A. S., and Kozak, K. Light microscopy applications in systems biology: opportunities and challenges. *Cell Communication and Signaling*, 11, 2013. doi: 10.1186/1478-811X-11-24.
- Arbelle, A. and Raviv, T. R. Microscopy cell segmentation via convolutional lstm networks. In *International Symposium on Biomedical Imaging*, 2019. doi: 10.1109/ISBI.2019.8759447.
- Bao, R., Al-Shakarji, N. M., Bunyak, F., and Palaniappan, K. Dmnet: Dual-stream marker guided deep network for dense cell segmentation and lineage tracking. In *International Conference on Computer Vision Workshops*, 2021. doi: 10.1109/ICCVW54120.2021.00375.
- Belyaev, I., Praetorius, J.-P., Medyukhina, A., and Figge, M. T. Enhanced segmentation of label-free cells for automated migration and interaction tracking. *Cytometry Part A*, 2021. doi: 10.1002/cyto.a.24466.
- Bergmann, P., Meinhardt, T., and Leal-Taixe, L. Tracking without bells and whistles. In *International Conference on Computer Vision*, 2019. doi: 10.1109/ICCV.2019.00103.
- Bernardin, K. and Stiefelhagen, R. Evaluating multiple object tracking performance: the clear mot metrics. *Image and Video Processing*, 2008, 2008. doi: 10.1155/2008/246309.
- Chen, Y., Song, Y., Zhang, C., Zhang, F., O'Donnell, L., Chrzanowski, W., and Cai, W. Celltrack r-cnn: A novel end-to-end deep neural network for cell segmentation and tracking in microscopy images. In *Symposium on Biomedical Imaging*, 2021. doi: 10.1109/ISBI48211.2021.9434057.
- Eisenmann, M., Reinke, A., Weru, V., Tizabi, M. D., Isensee, F., Adler, T. J., Ali, S., Andrearczyk, V., Aubreville, M., Baid, U., Bakas, S., Balu, N., Bano, S., Bernal, J., Bodendstedt, S., Casella, A., Cheplygina, V., Daum, M., de Bruijne, M., Depeursinge, A., Dorent, R., Egger, J., Ellis, D. G., Engelhardt, S., Ganz, M., Ghatwary, N., Girard, G., Godau, P., Gupta, A., Hansen, L., Harada, K., Heinrich, M. P., Heller, N., Hering, A., Huault, A., Jannin, P., Kavur, A. E., Kodym, O., Kozubek, M., Li, J., Li, H., Ma, J., Martín-Isla, C., Menze, B., Noble, A., Oreiller, V., Padoy, N., Pati, S., Payette, K., Radsch, T., Rafael-Patiño, J., Bawa, V. S., Speidel, S., Sudre, C. H., van Wijnjen, K., Wagner, M., Wei, D., Yamlahi, A., Yap, M. H., Yuan, C., Zenk, M., Zia, A., Zimmerer, D., Aydogan, D. B., Bhattarai, B., Bloch, L., Brüngel, R., Cho, J., Choi, C., Dou, Q., Ezhov, I., Friedrich, C. M., Fuller, C. D., Gaire, R. R., Galdran, A., Faura, A. G., Grammatikopoulou, M., Hong, S., Jahanifar, M., Jang, I., Kadkhodamohammadi, A., Kang, I., Kofler, F., Kondo, S., Kuijff, H., Li, M., Luu, M., Martinčič, T., Morais, P., Naser, M. A., Oliveira, B., Owen, D., Pang, S., Park, J., Park, S.-H., Plotka, S., Puybareau, E., Rajpoot, N., Ryu, K., Saeed, N., Shephard, A., Shi, P., Štepec, D., Subedi, R., Tochon, G., Torres, H. R., Urien, H., Vilaça, J. a. L., Wahid, K. A., Wang, H., Wang, J., Wang, L., Wang, X., Wiestler, B., Wodzinski, M., Xia, F., Xie, J., Xiong, Z., Yang, S., Yang, Y., Zhao, Z., Maier-Hein, K., Jäger, P. F., Kopp-Schneider, A., and Maier-Hein, L. Why is the winner the best? In *Conference on Computer Vision and Pattern Recognition*, 2023. doi: 10.1109/CVPR52729.2023.01911.
- Eschweiler, D., Spina, T. V., Choudhury, R. C., Meyerowitz, E., Cunha, A., and Stegmaier, J. Cnn-based preprocessing to optimize watershed-based cell segmentation in 3d confocal microscopy images. In *International Symposium on Biomedical Imaging*, 2019. doi: 10.1109/ISBI.2019.8759242.
- Falk, T., Mai, D., Bensch, R., Çiçek, Ö., Abdulkadir, A., Marrakchi, Y., Böhm, A., Deubner, J., Jäckel, Z., Seiwald, K., et al. U-net: deep learning for cell counting, detection, and morphometry. *Nature Methods*, 16, 2019. doi: 10.1186/s12915-023-01780-2.
- Gawlikowski, J., Tassi, C. R. N., Ali, M., Lee, J., Humt, M., Feng, J., Kruspe, A., Triebel, R., Jung, P., Roscher, R., et al. A survey of uncertainty in deep neural networks. *Artificial Intelligence Review*, 2023. doi: 10.1007/s10462-023-10562-9.

- Granström, K., Svensson, L., Xia, Y., Williams, J., and García-Fernández, A. F. Poisson multi-bernoulli mixture trackers: Continuity through random finite sets of trajectories. In International Conference on Information Fusion, 2018. doi: 10.23919/ICIF.2018.8455849.
- Guerrero Peña, F. A., Marrero Fernandez, P. D., Tarr, P. T., Ren, T. I., Meyerowitz, E. M., and Cunha, A. J regularization improves imbalanced multiclass segmentation. In International Symposium on Biomedical Imaging, 2020. doi: 10.1109/ISBI45749.2020.9098550.
- Guo, T., Wang, Y., Solorio, L., and Allebach, J. P. Training a universal instance segmentation network for live cell images of various cell types and imaging modalities. arXiv preprint, 2022. doi: 10.48550/arXiv.2207.14347.
- Gupta, D. K., de Bruijn, N., Panteli, A., and Gavves, E. Tracking-assisted segmentation of biological cells. Conference on Neural Information Processing Systems Workshops, 2019. doi: 10.48550/arXiv.1910.08735.
- Hornakova, A., Kaiser, T., Rolinek, M., Rosenhahn, B., Swoboda, P., Henschel, R., and equal contribution), . Making higher order mot scalable: An efficient approximate solver for lifted disjoint paths. In International Conference on Computer Vision, 2021. doi: 10.1109/ICCV48922.2021.00627.
- Hossain, M. I., Gostar, A. K., Bab-Hadiashar, A., and Hossainezhad, R. Visual mitosis detection and cell tracking using labeled multi-bernoulli filter. In International Conference on Information Fusion, 2018. doi: 10.23919/ICIF.2018.8455486.
- Hu, T., Xu, S., Wei, L., Zhang, X., and Wang, X. Cell-Tracker: an automated toolbox for single-cell segmentation and tracking of time-lapse microscopy images. Bioinformatics, 37, 2021. doi: 10.1093/bioinformatics/btaa1106.
- Kalman, R. E. A new approach to linear filtering and prediction problems. Basic Engineering, 82, 1960.
- Lalit, M., Tomancak, P., and Jug, F. Embedding-based instance segmentation in microscopy. In Conference on Medical Imaging with Deep Learning, volume 143. PMLR, 2021.
- Lalit, M., Tomancak, P., and Jug, F. Embedseg: Embedding-based instance segmentation for biomedical microscopy data. Medical Image Analysis, 81, 2022. doi: 10.1016/j.media.2022.102523.
- Löffler, K., Scherr, T., and Mikut, R. A graph-based cell tracking algorithm with few manually tunable parameters and automated segmentation error correction. PLOS ONE, 16, 2021. doi: 10.1371/journal.pone.0249257.
- Lux, F. and Matula, P. Cell segmentation by combining marker-controlled watershed and deep learning. arXiv preprint, 2020. doi: 10.48550/arXiv.2004.01607.
- Löffler, K. and Mikut, R. Embedtrack—simultaneous cell segmentation and tracking through learning offsets and clustering bandwidths. IEEE Access, 10, 2022. doi: 10.1109/ACCESS.2022.3192880.
- Magnusson, K. E. G., Jaldén, J., Gilbert, P. M., and Blau, H. M. Global linking of cell tracks using the viterbi algorithm. Medical Imaging, 34, 2015. doi: 10.1109/TMI.2014.2370951.
- Mancusi, G., Panariello, A., Porrello, A., Fabbri, M., Calderara, S., and Cucchiara, R. Trackflow: Multi-object tracking with normalizing flows. In International Conference on Computer Vision, 2023. doi: 10.1109/ICCV51070.2023.00874.
- Maška, M., Ulman, V., Svoboda, D., Matula, P., Matula, P., Ederra, C., Urbiola, A., España, T., Venkatesan, S., Balak, D. M., Karas, P., Bolcková, T., Štreitová, M., Carthel, C., Coraluppi, S., Harder, N., Rohr, K., Magnusson, K. E. G., Jaldén, J., Blau, H. M., Dzyubachyk, O., Křížek, P., Hagen, G. M., Pastor-Escuredo, D., Jimenez-Carretero, D., Ledesma-Carbayo, M. J., Muñoz-Barrutia, A., Meijering, E., Kozubek, M., and Ortiz-de Solorzano, C. A benchmark for comparison of cell tracking algorithms. Bioinformatics, 30, 2014. doi: 10.1093/bioinformatics/btu080.
- Maška, M., Ulman, V., Delgado-Rodriguez, P., Gómez de Mariscal, E., Necasova, T., Guerrero Peña, F. A., Ing Ren, T., Meyerowitz, E., Scherr, T., Löffler, K., Mikut, R., Guo, T., Wang, Y., Allebach, J., Bao, R., Al-Shakarji, N., Rahmon, G., Toubal, I. E., Palaniappan, K., and Ortiz-de Solorzano, C. The cell tracking challenge: 10 years of objective benchmarking. Nature Methods, 20, 2023. doi: 10.1038/s41592-023-01879-y.
- Matula, P., Maška, M., Sorokin, D. V., Matula, P., Ortiz-de Solorzano, C., and Kozubek, M. Cell tracking accuracy measurement based on comparison of acyclic oriented graphs. PLOS ONE, 10, 2015. doi: 10.1371/journal.pone.0144959.
- Murty, K. G. An algorithm for ranking all the assignments in order of increasing cost. Operations Research, 16, 1968. doi: 10.1287/opre.16.3.682.
- Nguyen, T. T. D., Vo, B.-N., Vo, B.-T., Kim, D. Y., and Choi, Y. S. Tracking cells and their lineages via labeled random finite sets. Signal Processing, 69, 2021. doi: 10.1109/TSP.2021.3111705.

- Payer, C., Štern, D., Feiner, M., Bischof, H., and Urschler, M. Segmenting and tracking cell instances with cosine embeddings and recurrent hourglass networks. *Medical Image Analysis*, 57, 2019. doi: 10.1016/j.media.2019.06.015.
- Reid, D. An algorithm for tracking multiple targets. *Automatic Control*, 1979. doi: 10.1109/TAC.1979.1102177.
- Rezatofghi, S. H., Gould, S., Vo, B. T., Vo, B.-N., Mele, K., and Hartley, R. Multi-target tracking with time-varying clutter rate and detection profile: Application to time-lapse cell microscopy sequences. *Medical Imaging*, 34, 2015. doi: 10.1109/TMI.2015.2390647.
- Ronneberger, O., Fischer, P., and Brox, T. U-Net: Convolutional Networks for Biomedical Image Segmentation. In *Medical Image Computing and Computer-Assisted Intervention*. Springer International Publishing, 2015. doi: 10.1007/978-3-319-24574-4_28.
- Scherr, T., Löffler, K., Böhlend, M., and Mikut, R. Cell segmentation and tracking using cnn-based distance predictions and a graph-based matching strategy. *PLOS ONE*, 15, 2020. doi: 10.1371/journal.pone.0243219.
- Schiegg, M., Hanslovsky, P., Kausler, B. X., Hufnagel, L., and Hamprecht, F. A. Conservation tracking. In *International Conference on Computer Vision*, 2013. doi: 10.1109/ICCV.2013.364.
- Sixta, T., Cao, J., Seebach, J., Schnittler, H., and Flach, B. Coupling cell detection and tracking by temporal feedback. *Machine Vision and Applications*, 31, 2020. doi: 10.1007/s00138-020-01072-7.
- Stegmaier, J. and Mikut, R. Fuzzy-based propagation of prior knowledge to improve large-scale image analysis pipelines. *PLOS ONE*, 12, 2017. doi: 10.1371/journal.pone.0187535.
- Stegmaier, J., Alshut, R., Reischl, M., and Mikut, R. Information fusion of image analysis, video object tracking, and data mining of biological images using the open source matlab toolbox gait-cad. *Biomedical Engineering*, 57, 2012. doi: 10.1515/bmt-2012-4073.
- Ulman, V., Maška, M., Magnusson, K. E., Ronneberger, O., Haubold, C., Harder, N., Matula, P., Matula, P., Svoboda, D., Radojevic, M., et al. An objective comparison of cell-tracking algorithms. *Nature Methods*, 14, 2017. doi: 10.1038/nmeth.4473.
- Vo, B.-T. and Vo, B.-N. Labeled random finite sets and multi-object conjugate priors. *Signal Processing*, 61, 2013. doi: 10.1109/TSP.2013.2259822.
- Wang, G., Li, W., Aertsen, M., Deprest, J., Ourselin, S., and Vercauteren, T. Aleatoric uncertainty estimation with test-time augmentation for medical image segmentation with convolutional neural networks. *Neurocomputing*, 338, 2019. doi: 10.1016/j.neucom.2019.01.103.
- Wang, J. and Lukasiewicz, T. Rethinking bayesian deep learning methods for semi-supervised volumetric medical image segmentation. In *Conference on Computer Vision and Pattern Recognition*, 2022. doi: 10.1109/CVPR52688.2022.00028.
- Zhou, Z., Wang, F., Xi, W., Chen, H., Gao, P., and He, C. Joint multi-frame detection and segmentation for multi-cell tracking. In *Conference on Image and Graphics*. Springer, 2019. doi: 10.1007/978-3-030-34110-7_36.
- Zhu, Y. and Meijering, E. Automatic improvement of deep learning-based cell segmentation in time-lapse microscopy by neural architecture search. *Bioinformatics*, 37, 2021. doi: 10.1093/bioinformatics/btab556.

A. Merging Gaussian Mixtures

The calculation of the motion probability density $P_{k-1|k}^{j,\mathcal{Z}}$ and the position probability density $P_{k|k}^{j,\mathcal{Z}}$ is described in Equation (1) and (2). Both densities are multivariate Gaussians $\mathcal{N}(\cdot; \mu_m, \Sigma_m)$ defined by mean and covariance that are derived by merging a Gaussian mixture model $\text{GMM} = \{(w_i, \mathcal{N}(\cdot; \mu_i, \Sigma_i))\}_{i=1}^N$. The following Equations formalize the merging of GMM into a single Gaussian:

$$w_m = \sum_{i=1}^N w_i \quad (8)$$

$$\mu_m = \frac{1}{w_m} \sum_{i=1}^N w_i \mu_i \quad (9)$$

$$\Sigma_m = \sum_i^C \frac{w_i}{w_m} (\Sigma_i + (\mu_i - \mu_m)(\mu_i - \mu_m)^\top) \quad (10)$$

B. Experimental Details

Our method introduced in the main paper requires some parameters that encode prior knowledge into the tracking system. This section gives further information about the parameter settings of the main paper.

During PMBM processing, we apply common methods to reduce the computational complexity of the algorithm. Association sampling is limited to the $A_{\max} = 7$ most likely associations. Sampling is also stopped, if the next hypothesis has a probability 100 times smaller than the most likely hypothesis. After updating, we merge hypotheses that have equal states. Equal states are given, if every object n in hypothesis $h_1 \in \mathcal{H}_{k|k}$ has a corresponding object m in hypothesis $h_2 \in \mathcal{H}_{k|k}$ described by the same spatial position with $\mu_{k|k}^{n,h_1} = \mu_{k|k}^{m,h_2}$ and $\Sigma_{k|k}^{n,h_1} = \Sigma_{k|k}^{m,h_2}$, and causes the same mitosis costs $c^{M,n,h_1} = c^{M,m,h_2}$. Furthermore, we only keep the most likely $H_{\max} = 150$ hypotheses and remove the unlikely ones. Every hypothesis with a likelihood smaller than 0.0005 is removed regardless of the cardinality H_k . Note that we normalize the remaining hypothesis likelihoods with softmax after every reduction operation.

A relevant parameter required by our mitosis cost contribution introduced in Section 4.3 is k_M that describes the minimal length of reasonable cell cycles. We decided to set conservative parameters, such that k_M is smaller than the shortest cell cycle in the training data. The following parameter k_M were chosen: DIC-C2DH-HeLa 30, Fluo-C2DL-MSK 20, Fluo-N2DH-GOWT1 20, BF-C2DL-HSC 180, Fluo-N2DL-HeLa 20, BF-C2DL-MuSC 80, PhC-C2DH-U373 50, PhC-C2DL-PSC 40, and Fluo-N2DH-SIM+ 30.

After tracking, we apply postprocessing that removes trajectories that are shorter than 5 frames in temporal length. We also interpolate if there are gaps between detected instance segmentation masks within a cell trajectory.

C. Poisson Multi-Bernoulli Mixture Tracker

The main paper introduces novel contributions to the Poisson Multi-Bernoulli Mixture Tracker (PMBM). Since the tracker is complex in its formal description, this section recapitulates the PMBM tracker without our contributions and formalizes specific realizations necessary to re-implement the tracker. The general probabilistic framework is introduced in (Granström et al., 2018). Thus, we do not give theoretical details if not necessary for the practical usage and try to focus on practically relevant formulations. For this recap, we assume object representations as points with 2D Gaussian spatial probability distributions $\mathcal{N}(\cdot; \mu, \Sigma)$ parameterized by mean μ and covariance Σ . This is called a Gaussian prior and allows to use conjugate priors (Vo & Vo, 2013) which simplifies the calculation.

The goal of the PMBM tracker is to optimally solve the tracking problem for a discrete time step k by finding the most likely state $\mathbf{x}_k \in \mathcal{X}$ of the distribution

$$\mathcal{PMBM}_{k|k}(\mathbf{x}_k) = \sum_{\mathbf{x}_k^d \cup \mathbf{x}_k^u = \mathbf{x}_k} \lambda_{k|k}^u(\mathbf{x}_k^u) \mathcal{H}_{k|k}(\mathbf{x}_k^d) = \lambda_{k|k}^u(\mathbf{x}_k^u) \sum_{\mathbf{x}_k^d = \mathbf{x}_k \setminus \mathbf{x}_k^u} \mathcal{H}_{k|k}(\mathbf{x}_k^d). \quad (11)$$

The state \mathbf{x}_k is a conjunction of a set of existing but currently undetected objects \mathbf{x}_k^u and a set of detected objects \mathbf{x}_k^d . An undetected object $t \in \mathbf{x}_k^u$ is assumed to exist but was not detected in a measurement up to timestep k . Undetected objects at

k are modeled with a Poisson point process

$$\lambda_{k|k}^u(\cdot) = \sum_{t=1}^{N_k^u} w_{k|k}^{u,t} \mathcal{N}(\cdot; \mu_{k|k}^{u,t}, \Sigma_{k|k}^{u,t}) \quad \text{parameterized with} \quad \left\{ \left(w_{k|k}^{u,t}, \mu_{k|k}^{u,t}, \Sigma_{k|k}^{u,t} \right) \right\}_{t=1}^{N_k^u} \quad (12)$$

with N_k^u objects that have an intensity $w_{k|k}^{u,t}$ reflecting the probability to exist and a spatial distribution characterized by $\mu_{k|k}^{u,t}$ and $\Sigma_{k|k}^{u,t}$. Objects that were detected at least once until step k (*a.k.a.* detected objects) are modeled in a set of multiple hypotheses in a multi-Bernoulli mixture density. Hypotheses can differ in the number of objects or their spatial distribution and are defined by

$$\mathcal{H}_{k|k}(\cdot) = \sum_{h=1}^{H_k} l_{k|k}^h \sum_{i=1}^{N_k^h} B_i(\cdot) \quad \text{parameterized with} \quad \left\{ \left(l_{k|k}^h, \left\{ \left(r_{k|k}^{i,h}, \mathcal{N}(\cdot; \mu_{k|k}^{i,h}, \Sigma_{k|k}^{i,h}) \right) \right\}_{i=1}^{N_k^h} \right) \right\}_{h=1}^{H_k} \quad (13)$$

in which $l_{k|k}^h$ is the log-likelihood of hypothesis h which contains N_k^h objects i modeled with Bernoullis B_i . A Bernoulli is characterized with its probability of existence $r_{k|k}^{i,h}$ and a 2D Gaussian spatial distribution \mathcal{N} . At timestep $k = 0$ before measuring the first observation, $\mathcal{H}_{0|0} = \{(1, \emptyset)\}$ is initialized with a single hypothesis without objects, and $\lambda_{0|0}^u$ is initialized with an arbitrary set reflecting prior knowledge about the field of view. If there is no prior knowledge, $\lambda_{0|0}^u$ can be initialized with a single Poisson distribution with a large spatial variance and an expected position in the center of the field of view.

To find the most likely states \mathbf{x}_k with $k \in \{1, \dots, K\}$, multiple operations are performed sequentially on the distribution $\mathcal{PMBM}_{k|k}$. First, new states $\lambda_{k+1|k}^u$ and $\mathcal{H}_{k+1|k}$ are **predicted** using prior information from $\lambda_{k|k}^u$ and $\mathcal{H}_{k|k}$. Then, based on new measurements \mathcal{Z}_{k+1} (*a.k.a.* detections), possible **association** hypotheses Ψ_k^h are created to associate detections from \mathcal{Z}_{k+1} to objects from $h \in \mathcal{H}_{k+1|k}$. Based on an association $\psi \in \Psi_k^h$ as well as the corresponding hypothesis $h \in \mathcal{H}_{k+1|k}$ and measurement \mathcal{Z}_{k+1} , a new hypothesis $f(h, \mathcal{Z}_{k+1}, \psi) \in \mathcal{H}_{k+1|k+1}$ is created by **updating** h . The new undetected objects state $\lambda_{k+1|k+1}^u$ is created using assumptions. To reduce the computational complexity, a **reduction** of $\lambda_{k+1|k+1}^u$ and $\mathcal{H}_{k+1|k+1}$ by removing unlikely hypotheses is performed. Finally, the most likely state \mathbf{x}_{k+1} is **estimated** using the log-likelihoods of the hypotheses and the probabilities of existence of the objects.

The next sections give detailed information and formulations of each operation. We want to mention that we describe the realization used in our implementation which can slightly be different in other works.

C.1. Prediction

At first, a new distribution $\mathcal{PMBM}_{k+1|k}$ given prior knowledge from $\mathcal{PMBM}_{k|k}$ is predicted. Necessary information is the spatially distributed probability of survival $P^S(\cdot)$, the probability of birth $P^B(\cdot)$, and the expected process noise $\mathbf{Q}_k^{\text{Mov}}$ used in a Kalman filter motion model. The probability of survival describes the likelihood, that an existing object in step k is also existing in step $k + 1$. If no explicit knowledge about the survival behavior is given, P^S can be set constant. We set $P^S = 1$, thus expecting objects to survive. The probability of birth is modeled as a Poisson point process and adds new elements to λ_k^u . Since the distribution is usually not easy to define, P^B can be set similar to $\lambda_{k=0}^u$, which means that we assume an equally distributed probability of new elements over time. Moreover, we define the process noise $\mathbf{Q}_{k|k}^{\text{Mov}} = \mathbf{I}\sigma_{\text{Mov}}^2$ to be equivalent to the average object movement σ_{Mov} per step. The undetected object and detected states for all hypotheses are updated according to the following steps.

Add new undetected object parameters:

$$\lambda_{k+1|k}^u = \lambda_{k|k}^u + P^B \quad (14)$$

Predict old undetected object parameters:

$$w_{k+1|k}^{u,t} = w_{k|k}^{u,t} P^S(\mu_{k|k}^{u,t}) \quad (15)$$

$$\mathcal{N}(\cdot; \mu_{k+1|k}^{u,t}, \Sigma_{k+1|k}^{u,t}) = \mathcal{N}(\cdot; \mu_{k|k}^{u,t}, \Sigma_{k|k}^{u,t} + \mathbf{Q}_{k|k}^{\text{Mov}}) \quad (16)$$

Predict detected object parameters:

$$r_{k+1|k}^{i,h} = r_{k|k}^{i,h} P^S(\mu_k^{i,h}) \quad (17)$$

$$\mathcal{N}(\cdot; \mu_{k+1|k}^{i,h}, P_{k+1|k}^{i,h}) = \mathcal{N}(\cdot; \mu_{k|k}^{i,h}, \Sigma_{k|k}^{i,h} + \mathbf{Q}_{k|k}^{\text{Mov}}). \quad (18)$$

C.2. Sample Associations

In every new timestep $k + 1$, a new measurement represented by a set of 2D Gaussian distributed detections $\mathcal{Z}_{k+1} = \{\mathcal{N}(\cdot, \mu_{k+1}^{j,\mathcal{Z}}, \Sigma_{k+1}^{j,\mathcal{Z}})\}_{j=1}^{N_{k+1}^{\mathcal{Z}}}$ with $N_{k+1}^{\mathcal{Z}}$ detections are given into the tracking system. This measurement is used to create possible association hypotheses between already-known objects and new detections. Formally, for each hypotheses $h \in \mathcal{H}_{k+1|k}$ with N_k^h Bernoullis, A_k^h new association hypotheses Ψ_k^h are created. For an association hypothesis $\psi \in \Psi_k^h$, we denote $\psi^j = i$ if detection j is assigned to object i and $\psi^j = u$ if j is unassigned because it is clutter or a new, previously undetected object. Theoretically, the cardinality A_k^h is very large, because every detection j potentially could be assigned to every object i , or assigned to be $\psi^j = u$. To reduce the computational burden that would be caused by a large A_k^h in further steps, A_k^h is limited to $A_k^h \leq A_{\max}$ by only sampling a subset of the most likely association hypotheses. To sample the subset, a detection-centric cost matrix for every ψ^j is defined as

$$\mathbf{C}_k^h = \begin{bmatrix} c_k^{1,1,h} & c_k^{1,2,h} & \dots & c_k^{1,N_k^h,h} & c_k^{1,u,h} & \infty & \dots & \infty \\ c_k^{2,1,h} & c_k^{2,2,h} & \dots & c_k^{2,N_k^h,h} & \infty & c_k^{2,u,h} & \dots & \infty \\ \vdots & \vdots & \ddots & \dots & \dots & \dots & \ddots & \dots \\ c_k^{N_{k+1}^{\mathcal{Z}},1,h} & c_k^{N_{k+1}^{\mathcal{Z}},2,h} & \dots & c_k^{N_{k+1}^{\mathcal{Z}},N_k^h,h} & \infty & \infty & \dots & c_k^{N_{k+1}^{\mathcal{Z}},u,h} \end{bmatrix} \quad (19)$$

and sampling methods like Murty's (Murty, 1968) or Gibbs sampling can be used to solve the one-to-one assignment problem.

The costs $c_k^{j,i,h}$ and $c_k^{j,u,h}$ of the cost matrix can be calculated with the Gaussian probability functions that describe the object and detection positions. Assuming that detection j is no measurement noise and not a new object, a scoring function s_k gives the likelihood that j is assigned to object i with

$$s_k(j, i, h) = \frac{P^{D,i} r_{k+1|k}^{i,h} \mathcal{N}\left(\mu_{k+1|k}^{i,h}; \mu_{k+1}^{j,\mathcal{Z}}, \Sigma_{k+1|k}^{i,h} + \Sigma_{k+1}^{j,\mathcal{Z}}\right)}{\underbrace{\sum_{i'} P^{D,i'} r_{k+1|k}^{i',h} \mathcal{N}\left(\mu_{k+1|k}^{i',h}; \mu_{k+1}^{j,\mathcal{Z}}, \Sigma_{k+1|k}^{i',h} + \Sigma_{k+1}^{j,\mathcal{Z}}\right)}_{\text{Already detected Objects}} + \underbrace{\sum_t P^{D,t} w_{k+1|k}^{u,t} \mathcal{N}\left(\mu_{k+1|k}^{u,t}; \mu_{k+1}^{j,\mathcal{Z}}, \Sigma_{k+1|k}^{u,t} + \Sigma_{k+1}^{j,\mathcal{Z}}\right)}_{\text{Currently undetected Objects}}} \quad (20)$$

where $P^{D,i} = P^D(\mu_{k+1|k}^{i,h})$ and $P^{D,t} = P^D(\mu_{k+1|k}^{u,t})$ are the probabilities of detection of object i and t , respectively. The probability of detection is often set constant due to no available prior knowledge. In our method, we use our contribution to define P^D . With the scoring function and the probability of $\lambda_k^{C,j}$ that j is clutter, the costs are defined as

$$c_k^{j,i,h} = -\log\left(\left(1 - \lambda_k^{C,j}\right) \cdot s_k(j, i, h)\right) \quad (21)$$

$$c_k^{j,u,h} = -\log\left(\left(1 - \lambda_k^{C,j}\right) \cdot \left(1 - \sum_i s_k(j, i, h)\right)\right) \quad (22)$$

To reduce the space of possible assignments Ψ_k^h , the costs corresponding to implausible assignments are set to $c_k^{i,j,h} = \infty$. In our implementation, we set $c_k^{i,j,h} = \infty$ if the Mahalanobis distance between i and j is too large, also known as gating. We set the maximal Mahalanobis distance to 3.

C.3. Update

After association sampling, there are A_k^h association hypothesis $\psi \in \Psi_k^h$ for every existing hypothesis $h \in \mathcal{H}_{k+1|k}$. The next paragraph describes the update of parameters in h given ψ , \mathcal{Z}_{k+1} , and the above defined P^D and λ^C .

Undetected objects that remain undetected:

$$w_{k+1|k+1}^{u,t} = w_{k+1|k}^{u,t} (1 - P^{D,t}) \quad (23)$$

$$\mu_{k+1|k+1}^{u,t} = \mu_{k+1|k}^{u,t} \quad (24)$$

$$\Sigma_{k+1|k+1}^{u,t} = \Sigma_{k+1|k}^{u,t} \quad (25)$$

New objects detected for the first time or Clutter: If a measurement j is not associated with an old object i , the measurement is either clutter or associated with a currently undetected object. Thus, we add a Bernoulli representing both possibilities to the current hypothesis h with parameters given by

$$\forall j : \psi^j = \mathbf{u} : r_{k+1|k+1}^{\text{new},h} = \frac{1 - \sum_i s_k(j, i, h)}{1 + \lambda_k^{\text{C},j} - \sum_i s_k(j, i, h)} \quad (26)$$

$$\forall j : \psi^j = \mathbf{u} : \mu_{k+1|k+1}^{\text{new},h} = \mu_{k+1}^{j,\mathcal{Z}} \quad (27)$$

$$\forall j : \psi^j = \mathbf{u} : \Sigma_{k+1|k+1}^{\text{new},h} = \Sigma_{k+1}^{j,\mathcal{Z}} \quad (28)$$

Associated measurements: If an object i is assigned to a measurement j , the object can be assumed to exist and the position can be updated with the Kalman filter given by

$$\forall i : \psi^j = i : r_{k+1|k+1}^{i,h} = 1 \quad (29)$$

$$\forall i : \psi^j = i : \mu_{k+1|k+1}^{i,h} = \mu_{k+1|k}^{i,h} + \mathbf{K}_{k+1}^{i,h} (\mu_{k+1}^{j,\mathcal{Z}} - \mu_{k+1|k}^{i,h}) \quad (30)$$

$$\forall i : \psi^j = i : \Sigma_{k+1|k+1}^{i,h} = (\mathbf{I} - \mathbf{K}_{k+1}^{i,h}) \Sigma_{k+1|k}^{i,h} \quad (31)$$

$$\text{with } \mathbf{K}_{k+1}^{i,h} = \Sigma_{k+1|k}^{i,h} (\Sigma_{k+1|k}^{i,h} + \Sigma_{k+1}^{j,\mathcal{Z}})^{-1} \quad (32)$$

Misdetected objects: If there is no associated measurement for object i , the new parameters are defined as

$$\forall i : j \nexists : \psi^j = i : r_{k+1|k+1}^{i,h} = \frac{r_{k+1|k}^{i,h} (1 - P^{\text{D},i})}{1 - r_{k+1|k}^{i,h} P^{\text{D},i}} \quad (33)$$

$$\forall i : j \nexists : \psi^j = i : \mu_{k+1|k+1}^{i,h} = \mu_{k+1|k}^{i,h} \quad (34)$$

$$\forall i : j \nexists : \psi^j = i : \Sigma_{k+1|k+1}^{i,h} = \Sigma_{k+1|k}^{i,h} \quad (35)$$

Posterior log weights: The posterior log-likelihood of a new hypothesis $f(h, \mathcal{Z}_{k+1}, \psi) \in \mathcal{H}_{k+1|k+1}$ created from h and ψ is depending on the update. It is a sum of the prior log-likelihood and the new log-likelihoods describing the probability of the aforementioned events. The formal definition of the new log-likelihood is given by

$$\tilde{l}_{k+1|k+1}^{h,\psi} = \underbrace{l_{k+1|k}^{h,\psi}}_{\text{Prior}} + \underbrace{\sum_{i:j \nexists : \psi^j = i} l_{k+1}^{u,i,h}}_{\text{Misdetection}} + \underbrace{\sum_{j:\psi^j \neq \mathbf{u}} l_{k+1}^{j,\psi^j,h}}_{\text{Assoc. Measurements}} + \underbrace{\sum_{j:\psi^j = \mathbf{u}} l_{k+1}^{j,u}}_{\text{Clutter or pot. new Objects}} \quad (36)$$

$$l_{k+1}^{j,u,h} = \log \left(\underbrace{\lambda_k^{\text{C},j}}_{\text{Clutter}} + \underbrace{(1 - \lambda_k^{\text{C},j}) \cdot \left(1 - \sum_i s_k(j, i, h)\right)}_{\text{Previously undetected}} \right) \quad (37)$$

$$l_{k+1}^{j,i,h} = \log \left((1 - \lambda_k^{\text{C},j}) \cdot s_k(j, i, h) \right) + \log \left(r_{k+1|k}^{i,h} P^{\text{D},i} \right) \quad (38)$$

$$l_{k+1}^{u,i,h} = \log \left(1 - r_{k|k-1}^{i,h} P^{\text{D},i} \right) \quad (39)$$

Table 4. Benchmark on Technical Measures according to the CTC (Maška et al., 2023). Colored cells show the performance of top #k state-of-the-art methods. Baseline rows compare the vanilla EmbedTrack (Löffler & Mikut, 2022) to the results evaluated with our approach. **Bold** numbers indicate that we outperform the baseline and underlined numbers indicate that our approach is the new state-of-the-art. Affiliations and references for the method names can be found in Tab. 5.

		Method									
[%]		BF-C2DL- HSC	BF-C2DL- MuSC	DIC-C2DL- HeLa	Fluo-C2DL- MSC	Fluo-N2DH- GOWT1	Fluo-N2DL- HeLa	PhC-C2DH- U373	PhC-C2DL- PSC	Fluo-N2DH- SIM+	Method
OP _{CTB}	Top #1	90.7	87.8	90.9	75.9	93.8	95.6	95.4	85.5	90.5	KIT-GE (3)
	Top #2	90.6	87.5	90.4	74.0	94.1	95.3	95.1	85.4	90.3	KIT-GE (4)
	Top #3	90.1	87.0	89.8	71.0	94.0	95.3	95.1	85.1	89.6	KTH-SE (1)
	Baseline	90.6	87.8	87.9	63.6	94.0	94.9	95.1	85.4	90.5	BGU-IL (4)
	Ours	<u>90.7</u>	87.5	88.3	62.9	94.1	94.7	95.1	85.1	90.3	BGU-IL (5)
SEG	Top #1	82.6	78.2	86.3	65.5	93.1	92.3	92.4	74.3	83.0	FR-GE (3)
	Top #2	82.6	77.8	85.3	64.9	92.9	92.2	92.3	74.0	82.9	TUG-AT
	Top #3	81.8	77.4	85.2	64.5	92.9	91.9	92.2	73.8	82.5	ND-US (1)
	Baseline	82.6	78.2	82.4	57.9	92.9	90.6	92.0	74.0	83.0	DREX-US
	Ours	82.6	77.8	82.6	56.8	92.9	90.3	92.0	73.8	82.9	UVA-NL
TRA	Top #1	98.8	97.4	95.5	87.3	97.9	99.3	98.5	96.8	97.9	RWTH-GE (1)
	Top #2	98.7	97.1	95.4	83.9	97.6	99.2	98.2	96.7	97.8	MU-CZ (2)
	Top #3	98.5	97.1	95.4	78.8	96.7	99.1	98.2	96.6	97.7	PURD-US (*)
	Baseline	98.5	97.4	93.4	69.3	95.1	99.2	98.2	96.8	97.9	DESU-US
	Ours	<u>98.8</u>	97.1	93.9	69.1	95.3	99.0	98.1	96.5	97.7	MU-US (2)

C.4. Reduction

With associating and updating $\mathcal{H}_{k+1|k}$ to $\mathcal{H}_{k+1|k+1}$, the cardinality $H_{k+1|k+1} \geq H_{k+1|k}$ grows exponentially over time. To reduce the computational burden in practical computation, the cardinality of $\mathcal{H}_{k+1|k+1}$ is reduced by **Merging**, **Capping**, and **Pruning**. The operations are described in the following.

If there are multiple hypotheses in $\mathcal{H}_{k+1|k+1}$ that have (approximately) the same state, they can be merged into a single hypothesis. Usually, the most likely hypothesis is kept and the corresponding log-likelihood is updated, such that it reflects the accumulated probability of all merged hypotheses. In our implementation, we only merge hypotheses iff they are entirely equal.

Another approach is capping, in which the hypotheses with the lowest probability are removed from $\mathcal{H}_{k+1|k+1}$ until $H_k \leq H_{\max}$. In our experiments, we set $H_{\max} = 150$.

Pruning is applied to remove very unlikely hypotheses. If the log-weight $l_{k+1|k+1}^h \leq \Gamma$ of hypothesis $h \in \mathcal{H}_{k+1|k+1}$ is too high, the hypothesis is removed. We set $\Gamma = \log(0.0005)$ in our implementation. Furthermore, detected or undetected objects that have a small probability of existence $r_{k+1|k+1}^{h,i}$ or $w_{k+1|k+1}^{u,t}$ should be removed to reduce computation. We remove objects with $r_{k+1|k+1}^{h,i} < 0.01$ and $w_{k+1|k+1}^{u,t} < 0.0001$.

After pruning or capping, the log-likelihoods need to be normalized by the softmax function to avoid numerical instabilities.

C.5. Estimation

To get the most likely state \mathbf{x}_k with knowledge up to time k , the most likely hypothesis $h \in \mathcal{H}_k$ can be selected by the log-likelihoods $l_{k|k}^h$. The hypothesis consists of objects that potentially could exist. The probability of existence is determined by $r_{k|k}^{h,i}$. Thus, unlikely objects in h with $r_{k|k}^{h,i} < 0.5$ can be considered as not existing and removed from the hypothesis and all other objects can be considered as existing.

Table 5. Details to related methods that are used in the main paper according to the naming conventions of the CTC (Maška et al., 2023). Methods that are referenced with *CTC Report* have no associated scientific publication but are described in detail in technical reports accessible at <http://celltrackingchallenge.net/participants/>.

Tag	Affiliation	Country	City	Reference
KIT-GE (1)	Karlsruhe Institute of Technology	Germany	Karlsruhe	(Stegmaier et al., 2012)
KIT-GE (2)	Karlsruhe Institute of Technology	Germany	Karlsruhe	(Löffler et al., 2021)
KIT-GE (3)	Karlsruhe Institute of Technology	Germany	Karlsruhe	(Scherr et al., 2020)
KIT-GE (4)	Karlsruhe Institute of Technology	Germany	Karlsruhe	(Löffler & Mikut, 2022)
KTH-SE (1)	KTH Royal Institute of Technology, RaySearch Laboratories	Sweden	Stockholm	(Magnusson et al., 2015)
KTH-SE (1*)	KTH Royal Institute of Technology, RaySearch Laboratories	Sweden	Stockholm	(Magnusson et al., 2015)
KTH-SE (3)	KTH Royal Institute of Technology, RaySearch Laboratories	Sweden	Stockholm	(Magnusson et al., 2015)
KTH-SE (5)	KTH Royal Institute of Technology, RaySearch Laboratories	Sweden	Stockholm	(Magnusson et al., 2015)
BGU-IL (1)	Ben-Gurion University of the Negev	Israel	Beer-Sheva	(Arbelle & Raviv, 2019)
BGU-IL (4)	Ben-Gurion University of the Negev	Israel	Beer-Sheva	(Arbelle & Raviv, 2019)
BGU-IL (5)	Ben-Gurion University of the Negev	Israel	Beer-Sheva	CTC Report
HD-GE (BMCV) (1)	Biomedical Computer Vision Group, University of Heidelberg	Germany	Heidelberg	CTC Report
HD-GE (IWR)	Interdisciplinary Center for Scientific Computing, University of Heidelberg	Germany	Heidelberg	(Schiegg et al., 2013)
FR-GE (2)	University of Freiburg	Germany	Freiburg	(Ronneberger et al., 2015)
FR-GE (3)	University of Freiburg	Germany	Freiburg	(Falk et al., 2019)
HKI-GE (5)	Hans Knöll Institute	Germany	Jena	(Belyaev et al., 2021)
THU-CN (2)	Tsinghua University	China	Beijing	(Hu et al., 2021)
TUG-AT	Graz University of Technology	Austria	Graz	(Payer et al., 2019)
USYD-AU	University of Sydney	Australia	Sydney	(Chen et al., 2021)
ND-US (1)	University of Notre Dame	USA	Notre Dame	CTC Report
DREX-US	Drexel University	USA	Philadelphia	CTC Report
IMCB-SG (1)	Institute of Molecular and Cell Biology	Singapore	Singapore	CTC Report
UVA-NL	University of Amsterdam	The Netherlands	Amsterdam	(Gupta et al., 2019)
HIT-CN (1)	Harbin Institute of Technology	China	Shenzhen	(Zhou et al., 2019)
CVUT-CZ	Czech Technical University in Prague	Czech Republic	Prague	(Sixta et al., 2020)
RWTH-GE (1)	RWTH Aachen University	Germany	Aachen	(Eschweiler et al., 2019)
MU-CZ (2)	Masaryk University	Czech Republic	Brno	(Lux & Matula, 2020)
PURD-US (*)	Purdue University	USA	West Lafayette	(Guo et al., 2022)
DESU-US	Delaware State University	USA	Dover	CTC Report
MU-US (2)	University of Missouri	USA	Columbia	CTC Report
MU-US (3)	University of Missouri	USA	Columbia	(Bao et al., 2021)

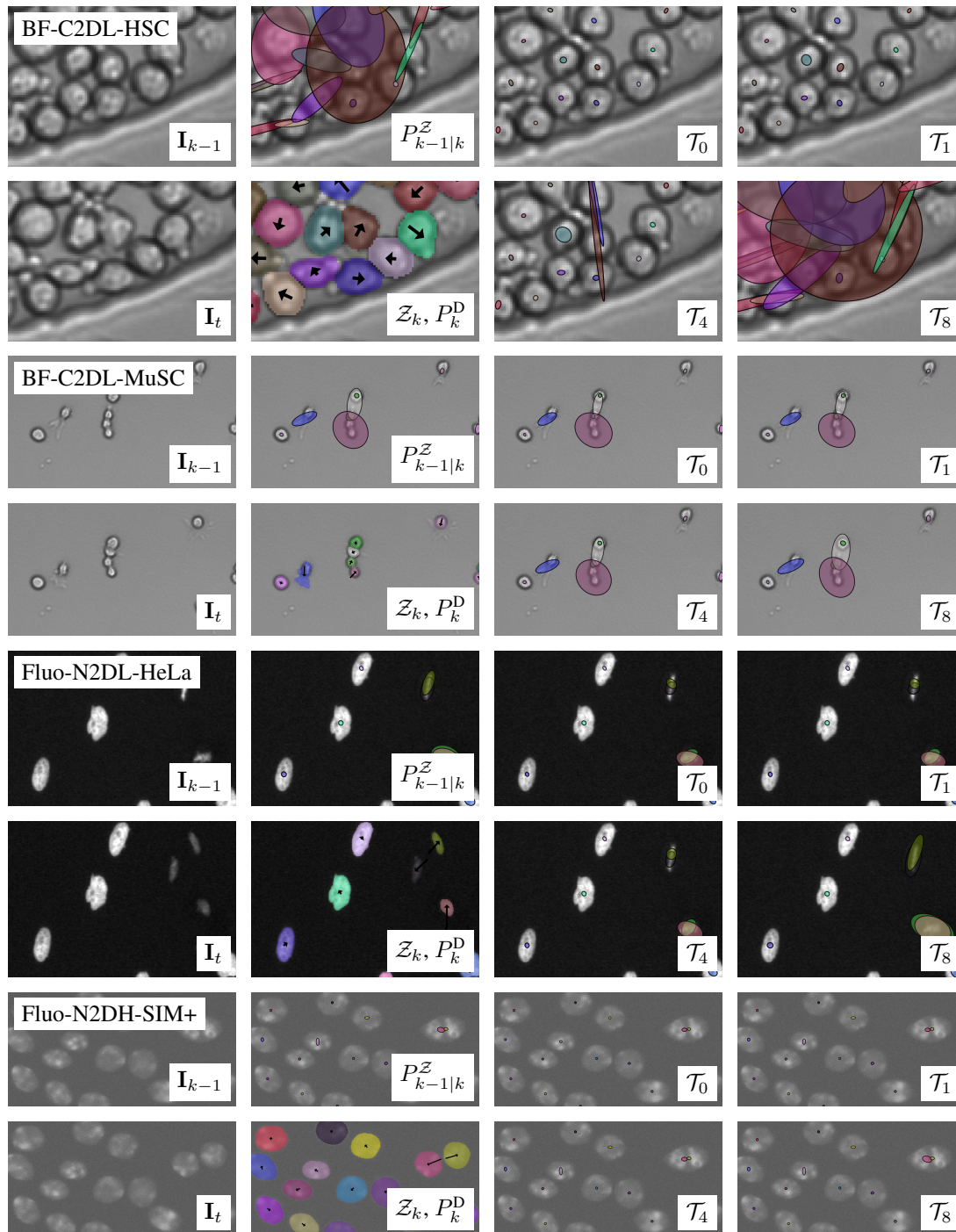


Figure 5. Supplementary examples of the motion uncertainty prediction depending on the test-augmentation shift as described in Figure 2.

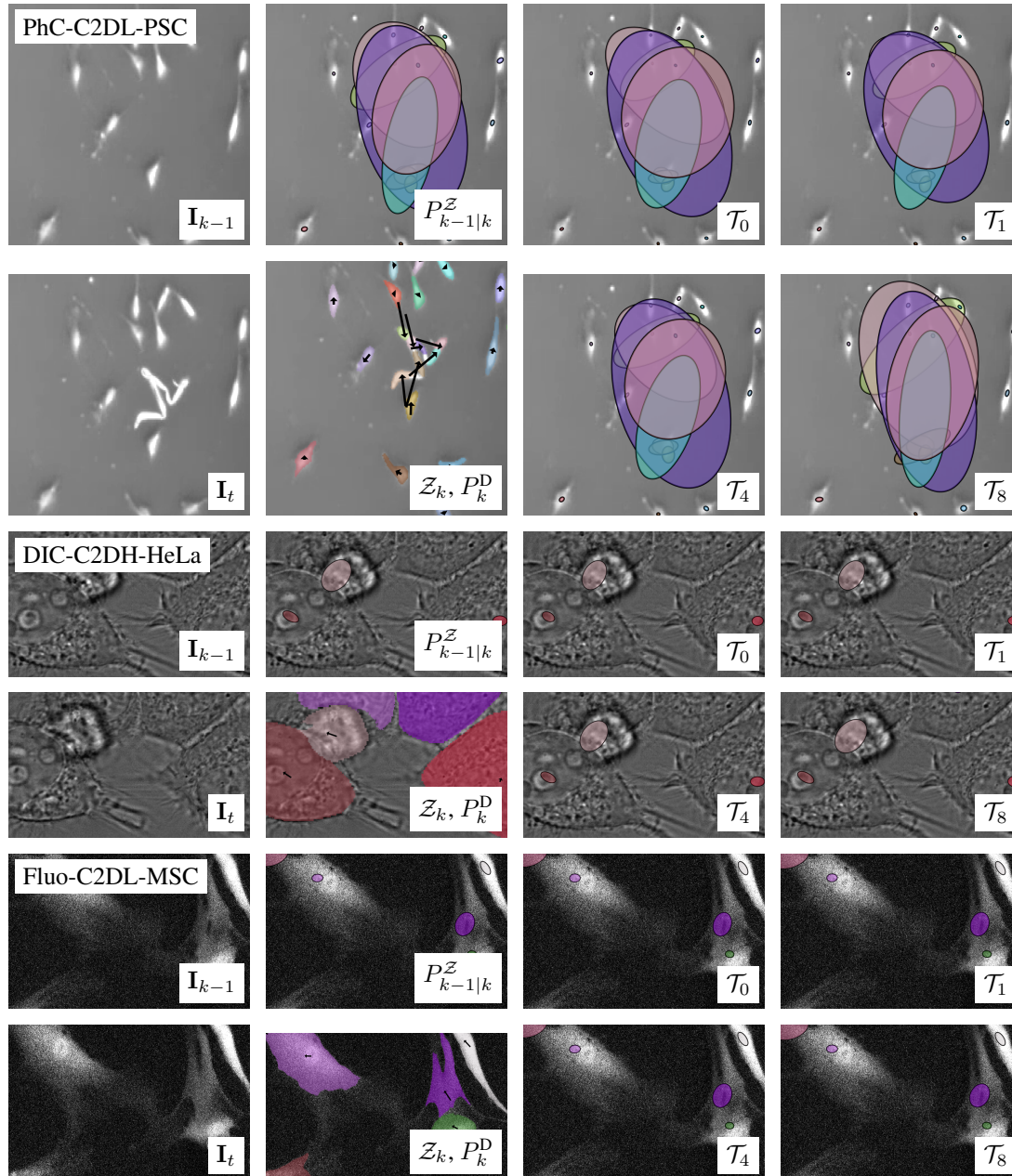


Figure 6. Supplementary examples of the motion uncertainty prediction depending on the test-augmentation shift as described in Figure 2.

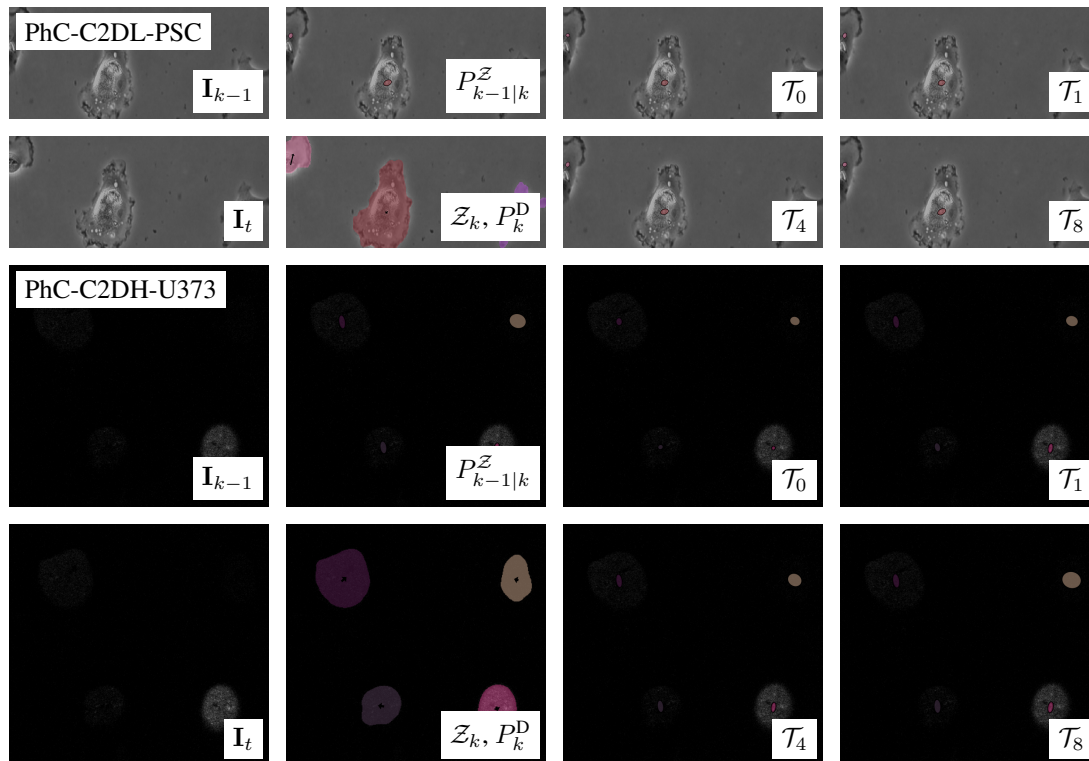


Figure 7. Supplementary examples of the motion uncertainty prediction depending on the test-augmentation shift as described in Figure 2.

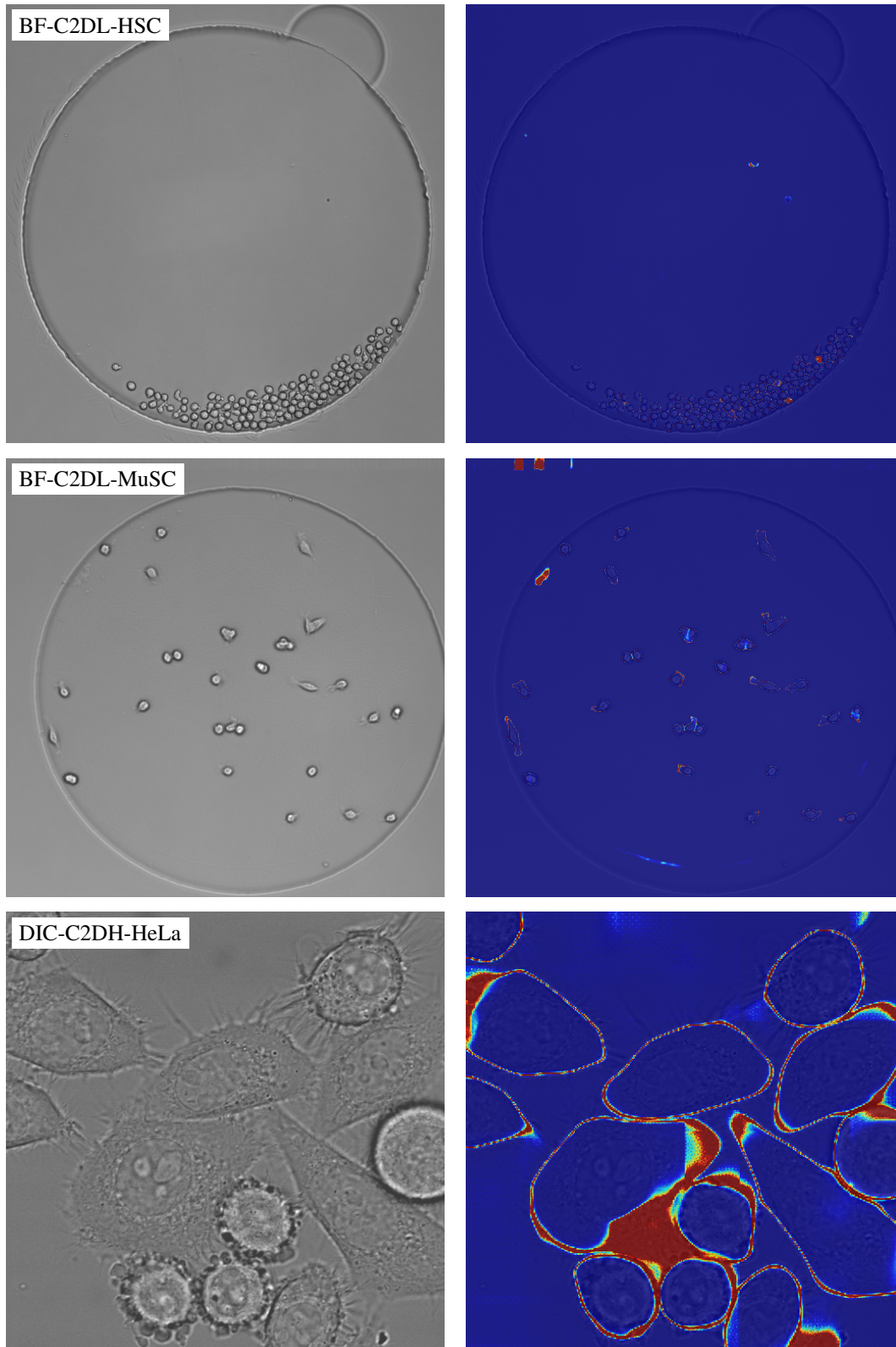


Figure 8. Supplementary examples of the probability of detection as described in Figure 1.

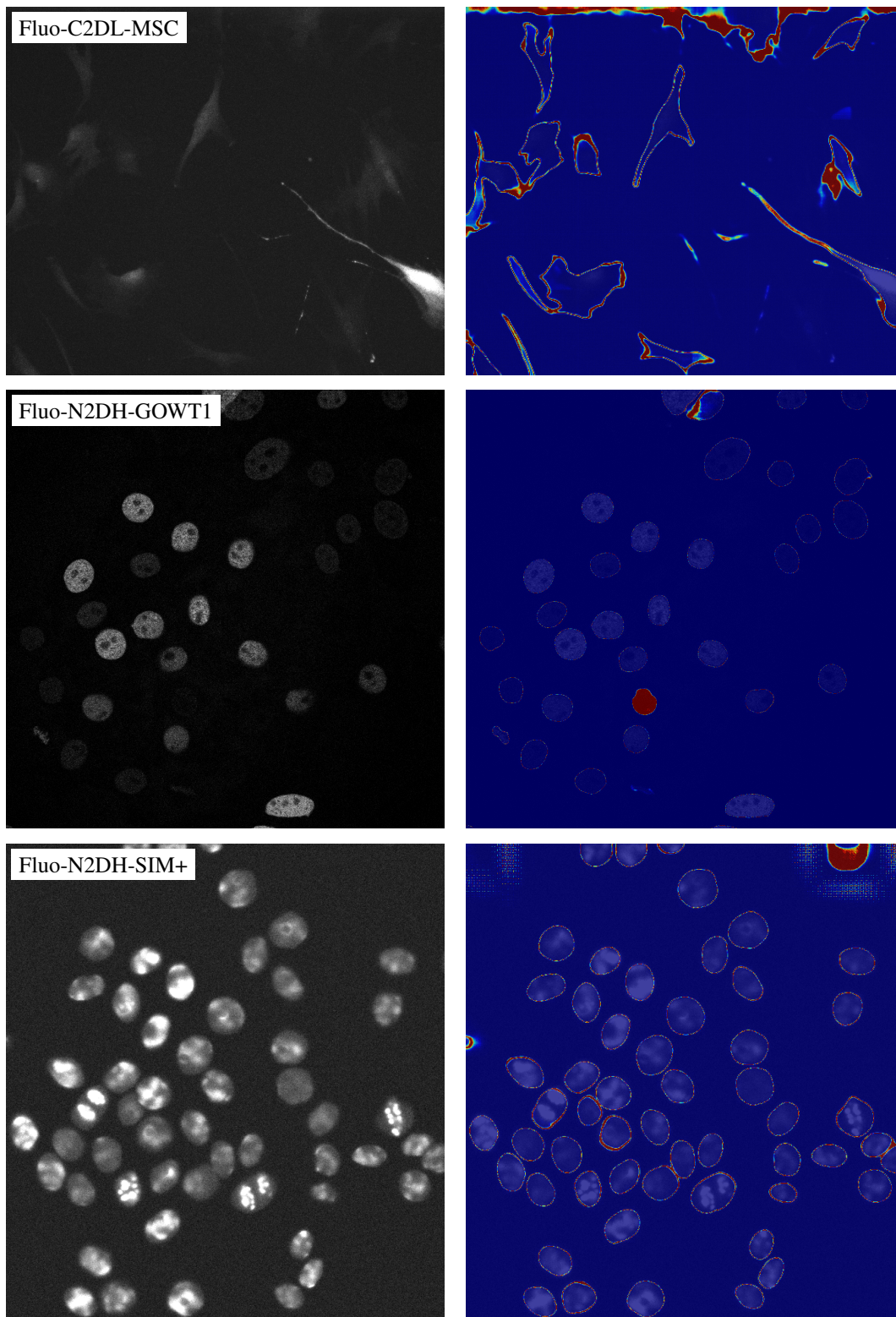


Figure 9. Supplementary examples of the probability of detection as described in Figure 1.

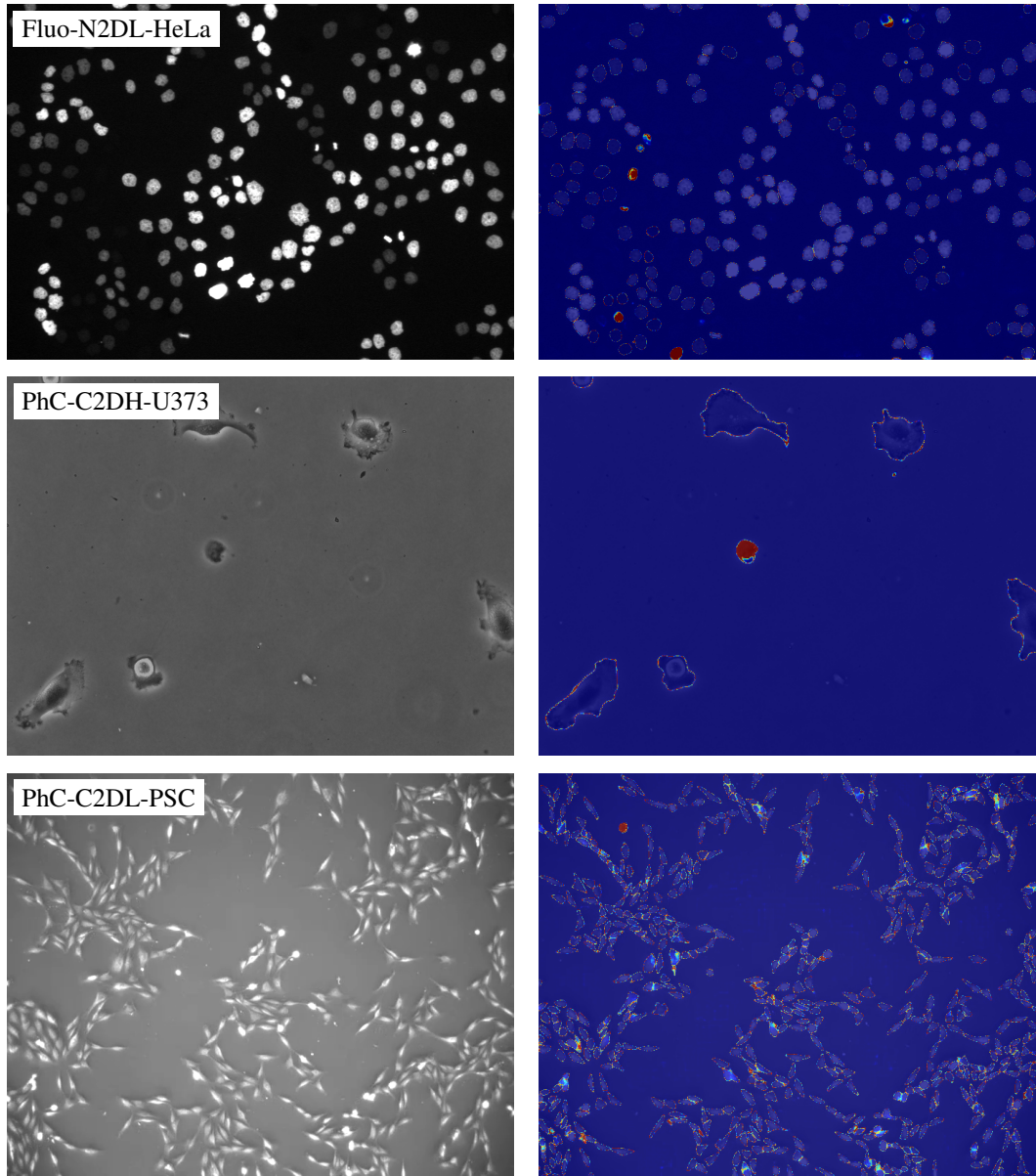


Figure 10. Supplementary examples of the probability of detection as described in Figure 1.